Virtual memory T-cells orchestrate extra-lymphoid responses conducive to resident memory

Shiyue Hou[1,2,3]†, Tiange Shao[1,2,3]†, Tianyang Mao[4], Jingwen Shi[1,2,3,4], Jiahui Sun[1,2,3], Miao Mei[1,5], Xu Tan[1,5], Hai Qi[1,2,3,4,6,7]*

[1]Tsinghua-Peking Center for Life Sciences

[2]Laboratory of Dynamic Immunobiology, Institute for Immunology

[3]Department of Basic Medical Sciences, School of Medicine

[4]School of Life Sciences

[5]School of Pharmacological Sciences

[6]Beijing Key Laboratory for Immunological Research on Chronic Diseases

[7]Beijing Frontier Research Center for Biological Structure

Tsinghua University, Beijing 100084, China

† These authors contribute equally to this work.

* Correspondence to qihai@tsinghua.edu.cn

Abstract

A primary immune response is initiated in secondary lymphoid organs. Virtual memory CD8$^+$ T (T$_{VM}$) cells are antigen-inexperienced T cells of a central-memory phenotype, acquired through self antigen-driven homeostatic proliferation. Unexpectedly, we find that T$_{VM}$ cells are composed of CCR2$^+$ and CCR2$^-$ subsets that differentially elaborate a spectrum of effector- and memory-poised functions directly in the tissue. During a primary flu infection, T$_{VM}$ cells rapidly infiltrate the lungs in the first day post-infection and promote early viral control. T$_{VM}$ cells that recognize viral antigen are retained in the tissue, clonally expand independent of secondary lymphoid organs, and give rise to tissue-resident memory cells. By orchestrating an extra-lymphoid primary response, heterogenous T$_{VM}$ cells bridge innate reaction and adaptive memory directly in the infected tissue.

Introduction

The memory T cell compartment formed following primary infection is heterogenous and composed of cells that reside in the tissue of original pathogen entry, or tissue-resident memory T (T_{RM}) cells, and those that can circulate in the blood and secondary lymphoid organs, or central memory T (T_{CM}) cells (1, 2). Increasing evidence supports a key role of T_{RM} cells for orchestrating effective defense against reinfection in the local tissue that they reside (3-7), although the precise route(s) by which T_{RM} cells develop in a primary infection is not well understood.

Apart from canonical, antigen-experienced memory T cells, some $CD8^+$ T cells may exhibit a memory phenotype without overt immunization or infection. For example, cells of a memory phenotype can arise in the thymus as "innate $CD8^+$ T cells" when Tec kinase-dependent pathways are compromised (8-11). Cells of a memory phenotype also develop from peripheral naïve T cells upon homeostatic proliferation in physiological lymphopenia (12-14). These cells, unlike true memory T cells that develop in response to foreign antigen, express only low levels of CD49d and are termed virtual memory T (T_{VM}) cells (15, 16). Consistent with dependence on exposure to self antigen, T_{VM} cells tend to develop from naïve T cells expressing higher CD5 levels (14). The transcription factor EOMES and homeostatic cytokine interleukin-15 are important intrinsic and extrinsic factors for T_{VM} development, respectively (17, 18).

Upon antigen challenge, T_{VM} cells display features that are distinct from either naïve or true memory counterparts in terms of proliferative capacity and differentiation toward short-lived effector cells versus long-lived memory (14, 16, 19). However, it is not clear whether T_{VM} cells are a homogenous population of cells conferred with identical functional potentials. It is also not clear how, as a polyclonal population harboring a diverse antigen receptor repertoire, T_{VM} cells would contribute to an antigen-specific protective response to infection. In this study, we find that T_{VM} cells are heterogenous in terms of effector and memory potentials and that these cells can rapidly infiltrate the site of infection to orchestrate a primary response directly in the tissue that gives rise to T_{RM} cells.

Results

Virtual memory T cells rapidly infiltrate lung upon flu infection

We analyzed immune cell infiltration into the lung before and after intranasal infection with the PR8 influenza A virus. Whereas there were few $CD8^+$ T cells in the lungs of specific pathogen-free (SPF) B6 mice, a large number of $CD8^+$ T cells appeared in the lung tissue as early as 18 hours after infection (Figure 1A-C). While cells of a $CD62L^-CD44^+$ effector memory (T_{EM}) phenotype are expected to migrate into the tissue, a larger fraction of lung-infiltrating $CD8^+$ T cells had a $CD62L^+CD44^+$ central memory

(T_{CM}) phenotype (Figure 1D-E). In SPF mice, CD49d separates *bona fide* T_{CM} cells that are generated in response to foreign agonistic antigen from virtual memory CD8$^+$ T (T_{VM}) cells that have not experienced foreign antigen but nonetheless acquired the CD62L$^+$CD44$^+$ phenotype through self antigen-driven homeostatic proliferation (*12-14, 16, 20*). Interestingly, lung-infiltrating T_{CM}-like cells were mostly CD49d$^-$, similar to those CD62L$^+$CD44$^+$ in the blood (Figure 1F-G; Figure S1A-B). Therefore, upon infection, lung rapidly recruits T_{VM} cells. While of increased affinities to self antigen (*16, 21*), T_{VM} cells harbor a polyclonal repertoire that contains a wide range of foreign specificities (*12, 13*). T cells of increased self affinities in the thymus may carry out a stronger response against foreign antigen in the periphery (*22*). Subsequently, we investigated how T_{VM} cells could rapidly infiltrate inflamed tissues and whether they could orchestrate an adaptive response directly in the tissue site of infection.

T_{VM} cells can be divided into two subsets according to CCR2 expression

T_{VM} cells in SPF mice could be gated as CD62L$^+$CD44$^+$ or CD44$^+$CD122$^+$, as we confirmed that either gating strategy identifies the CD49d$^-$ population (Figure S2). Using the CD62L$^+$CD44$^+$ gating in SPF mice, we profiled chemokine receptor expression by T_{VM} cells. Compared to naïve (T_N) cells, T_{VM} cells highly expressed mRNA for a suite of inflammatory chemokine receptors, prominently including CCR2, CCR5 and CXCR3 (Figure 2A). They also expressed a homeostatic chemokine receptor CXCR5, which has been increasingly associated with CD8$^+$ T-cell stemness (*23-26*). By flow cytometry, essentially all T_{VM} cells highly expressed CXCR3, similar to previous reports (*14, 19*), and most expressed CCR5 and CXCR5 in a relatively uniform manner. Conversely, CCR2 was highly expressed by 30-40% of T_{VM} cells, as detected by the MC21 anti-CCR2 antibody (Figure 2B). Albeit not well characterized in T cells, CCR2 is utilized by monocytes to rapidly infiltrate inflammatory tissue sites (*27*). This led us to hypothesize that CCR2$^+$ T_{VM} cells represent a specialized state or subset poised for tissue-site functions.

CCR2$^+$ T_{VM} cells likely develop due to homeostatic exposure to self antigen

CCR2$^+$ T_{VM} cells appeared in 1-week-old mice, as early as the initial wave of T_{VM} cells previously reported (*13*), and represented a stable fraction of total T_{VM} cells thereafter (Figure 2C). Following adoptive transfer into naïve hosts, CCR2$^+$ T_{VM} cells and their CCR2$^-$ counterparts were able to maintain respective phenotypes for at least 3 weeks (Figure 2D), suggesting that they were either epigenetically stable and/or being continuously exposed to an environment conducive to their phenotype maintenance *in vivo*. We confirmed that germ-free mice contain T_{VM} cells, as previously reported (*12*), and found that such mice also harbored a similar population of CCR2$^+$ T_{VM} cells (Figure

2E). We then took advantage of the CCR2 loss-of-function knock-in RFP reporter strain (*28*) to isolate polyclonal naïve $Ccr2^{rfp/+}$ T cells (purity shown in Figure S3A). These naïve T cells gave rise to CCR2$^+$ T$_{VM}$ cells, as identified by RFP fluorescence, 21 days after transfer into sub-lethally irradiated CD45.1 mice (Figure 2F). Similarly, naïve TCR transgenic OT-I T cells could also generate CCR2$^+$ T$_{VM}$ cells in lymphopenic hosts (Figure S3B-E).

To further probe the relationship of CCR2 upregulation and self ligand recognition, we took advantage of OT-I T cells and one of its known positive-selecting peptides, β-catenin-derived Catnb$_{329-336}$ (*29*). We found that *ex vivo* Catnb$_{329-336}$ stimulation was sufficient for inducing naïve OT-I T cells to become CD62L$^+$CD44$^+$ and significantly upregulate CCR2, particularly in the presence of IL-7 and IL-15 (Figure 2G-H). Catnb$_{329-336}$ stimulation also led to modest CD25 upregulation (Figure 2H). Interestingly, agonistic OVA$_{257-264}$ stimulation increased CCR2 expression at the picomolar range but became inhibitory beyond sub-nanomolar concentrations, whereas this same dose range permitted monotonic upregulation of CD25 (Figures 2G-H). These data suggest that CCR2 expression by T cells and the appearance of CCR2$^+$ T$_{VM}$ cells could be a consequence of exposure to self antigen and homeostatic cytokine environment.

Surface expression of CD5, which is determined in the thymus and reflects T-cell affinity to self antigen during selection (*30-33*), was higher on T$_{VM}$ cells than naïve T cells, as expected (*14, 22*), but was not different between CCR2$^+$ and CCR2$^-$ T$_{VM}$ cells (Figure S4A-B). Upon breeding Nur77-GFP reporter mice with the $Ccr2^{rfp/+}$ strain, we found a lower Nur77 level in CCR2$^+$ than in CCR2$^-$ T$_{VM}$ cells (Figure S4C-D). Therefore, while exposure to self antigen in the periphery likely generates CCR2$^+$ T$_{VM}$ cells, CCR2$^+$ T$_{VM}$ cells are not necessarily more reactive to self antigen than CCR2$^-$ T$_{VM}$ cells.

T$_{VM}$ cells are polyclonal in nature and contain virtually all antigen specificities tested (*12*). We found that, similar to polyclonal B6 mice, both OT-I and P14 TCR transgenic strains harbored a CCR2$^+$ T$_{VM}$ population (Figure S4E-F), although CD5 levels were varied among these cells (Figure S4G-H). Using a tetramer enrichment protocol, we could detect CCR2$^+$ T$_{VM}$ and CCR2$^-$ T$_{VM}$ cells in D^b-NP$_{366-374}$- and D^b-PA$_{224-233}$-specific precursors (Figure S5). Based on surface staining, CCR2$^+$ T$_{VM}$, CCR2$^-$ T$_{VM}$ cells, and naïve T cells in B6 mice also displayed a similarly diverse TCR Vβ usage, distinct from that of CD62L$^-$CD44$^+$ effector memory (T$_{EM}$) cells in the same mice (Figure 2I). For most of Vβ families tested, CCR2$^+$ and CCR2$^-$ T$_{VM}$ cells also exhibited smaller variations among individual mice than did T$_{EM}$ cells, consistent with the idea that both T$_{VM}$ subsets are shaped more by antigen shared among all the animals rather than by individual experience of different external antigen.

The CCR2$^+$ T$_{VM}$ cells are better poised for effector functions and tissue infiltration

Consistent with a more effector-ready state, CCR2$^+$ T$_{VM}$ cells expressed lower levels of T-zone-homing receptor CCR7 but higher levels of all the other inflammatory chemokine receptors (Figure 3A-B), CD44, and αL integrin (CD11a) (Figure 3C-D). Transcriptomic analyses by RNA sequencing also supported that CCR2$^+$ T$_{VM}$ cells have an enhanced effector potential compared to CCR2$^-$ T$_{VM}$ cells, as evidenced by their higher expression genes associated with cytotoxic function (e.g. *Klra4*, *Klra7*, *Klra13*, *Gzmm*, and *Ctka2a*) and inflammatory chemokines CCL4 and CCL5 (Figures 3E-F). CCR2$^+$ T$_{VM}$ cells more readily upregulated CD69, CD25 and IFN-γ upon brief anti-CD3/28 stimulation (Figure 3G) that was insufficient for activating naïve T cells. Like true memory T cells, T$_{VM}$ cells could rapidly produce IFN-γ in response to cytokine stimulation independently of TCR stimulation (*12, 34-36*) , and CCR2$^+$ T$_{VM}$ cells were superior in this bystander effector potential (Figure 3H).

To ascertain the functional relevance of these differences *in vivo*, we utilized a model of intracellular bacterial infection using recombinant *Listeria monocytogenes* expressing the OVA$_{257-264}$ epitope (*Lm*-OVA). In one set of experiments, we transferred 3×10^5 polyclonal CCR2$^+$ T$_{VM}$, CCR2$^-$ T$_{VM}$ or T$_N$ cells sorted from *Ccr2*$^{rfp/+}$ donors into *Cd8*$^{-/-}$ recipients that were subsequently challenged with a lethal dose (10^5 CFU) of bacteria. T$_N$, CCR2$^-$, and CCR2$^+$ T$_{VM}$ cells afforded increasingly better control of *Listeria* burdens in liver or spleen over the first 4 days (Figure 3I). In another set of experiments, we sort-purified T$_N$, CCR2$^-$ T$_{VM}$, or CCR2$^+$ T$_{VM}$ cells from *Ccr2*$^{rfp/+}$ CD45.1 OT-I mice. Upon transfer into B6 mice (10^3 per mouse) that were infected with *Lm*-OVA (10^4 CFU), these cells participated in antigen-specific responses against *Listeria* and developed into effector and memory precursor cells (*37*) (Figure 3J). By 21 days post infection, we found that CCR2$^+$ T$_{VM}$ cells gave rise to the most CD127^{lo}KLRG^{hi} short-lived effector cells (SLEC) but fewest CD127^{hi}KLRG^{lo} long-lived memory precursors (LLMP), while OT-I T$_N$ cells produced the most LLMPs (Figure 3J-K). These data demonstrate that T$_{VM}$ cells are functionally heterogenous and elaborate a spectrum of effector and progenitor potentials. CCR2$^+$ and CCR2$^-$ T$_{VM}$ subsets appear differentially poised at the two ends of the spectrum.

The CCR2$^+$ T$_{VM}$ subset dominates early lung infiltration

Consistent with intrinsically effector-prone features, CCR2$^+$ T$_{VM}$ cells were markedly over-represented in early lung-infiltrating T$_{VM}$ cells following PR8 infection (Figure 4A-B). To rule out rapid phenotypic conversion in the infected lung tissue and compare the two subsets more directly, we sort-isolated CCR2$^+$ and CCR2$^-$ T$_{VM}$ cells from CD45.1/2 and CD45.2 *Ccr2*$^{rfp/+}$ donor mice, respectively. These cells were co-transferred into CD45.1 mice one day after PR8 infection. In this model, we were able to track the two types of donor cells according to their CD45 congenic markers and at the same time to match their respective CCR2-RFP expression back to their pre-transfer states. We

found that the CCR2$^+$ T_{VM} subset outcompeted their CCR2$^-$ counterpart in infiltration to PR8-infected lungs and there was no evidence of phenotypic conversion (Figures 4C-D). CCR2$^+$ T_{VM} cells did not exhibit any numerical advantage in secondary lymphoid organs, ruling out a broad increase in engraftment efficiency of the CCR2$^+$ subset following adoptive transfer (Figure S6A-B). However, the lung-infiltrating advantage of the CCR2$^+$ T_{VM} subset was not absolute, implying CCR2 receptor itself might not drive the observed differences in T_{VM} cell recruitment. To directly test this point, we constructed CD45.1:CD45.2 $Ccr2^{rfp/rfp}$ and control CD45.1:CD45.2 $Ccr2^{+/+}$ mixed chimera. Following PR8 infection, wildtype and CCR2-deficient cells did not show significant differences in lung-infiltrating CD8$^+$ or T_{VM} cells, while CCR2 deficiency even conferred a slight advantage to T_{EM} infiltration (Figure 4E).

Lung infiltration of T_{VM} cells depends on CXCR3 and promotes early viral control

The CCR2$^+$ T_{VM} subset contained a larger fraction of CXCR3$^+$ cells, which also expressed a higher level of CXCR3 (Figure 3A-B; Figure S6C-D). CXCR3 can promote T-cell infiltration to the lung (*38*). After germline CXCR3 knockout (XR3KO) mice were infected with PR8, T_{VM} infiltration into the lung was severely reduced, but T_{EM} infiltration was not altered, while splenic T_{VM} or T_{EM} abundance did not change (Figure 4F-G). We further constructed $Cd8^{-/-}$:XR3KO (80:20) BM chimera to test a T-cell-intrinsic role for CXCR3. T_{VM} infiltration was markedly reduced in these chimera as compared to that in $Cd8^{-/-}$:WT (80:20) control chimera, while the abundance of splenic T_{VM} cells was concomitantly increased (Figure 4H-I). Without CXCR3, T_{EM} infiltration into the lung was not reduced but somewhat increased. This is consistent with the fact that T_{EM} cells expressed lower levels of CXCR3 (Figure S6E-F), and they may utilize additional chemokine receptors. Therefore, T_{VM} cells depend on CXCR3 to infiltrate the lung soon after influenza infection, and the over-representation of the CCR2$^+$ subset most likely resulted from its higher levels of CXCR3 expression.

The requisite role for CXCR3 in early T_{VM} but not T_{EM} recruitment into the lung lent us a system to specifically test contribution of lung-infiltrating T_{VM} cells toward early viral control. We thus directly infected $Cd8^{-/-}$:XR3KO (80:20) and $Cd8^{-/-}$:WT (80:20) chimeric mice with the PR8 influenza virus. One day after the infection, mice were given daily FTY720 (i.p. 1 mg/kg) to block new entry of T_{VM} cells into the lung. When T_{VM} infiltration was severely limited, as in $Cd8^{-/-}$:XR3KO chimera, mice suffered a more severe loss of body weight and had significantly higher viral loads in the lung within the first 5 days after infection (Figure 4J). Consistent with their effects on viral control, lung-infiltrating T_{VM} cells expressed IFN-γ, as measured in IFN-γ IRES-YFP reporter mice, and also Granzyme B (Figures 4K-L). Taken together, these data suggest that an important function of T_{VM} cells is to infiltrate site of primary infection early on and

contribute to immediate pathogen control, a function better performed by the CCR2$^+$ subset.

Virus-specific cells in infiltrating T$_{VM}$ cells clonally expand in the lung

Given that T$_{VM}$ cells harbor a polyclonal repertoire, those early infiltrating cells could contain TCR specificities that can recognize viral antigen. Such cells may be able to clonally expand on antigen-presenting cells in the tissue to mount an antigen-specific response locally. To test this hypothesis, one day after PR8 infection, mice were injected with FTY720 daily to block new recruitment of T$_{VM}$ cells into the lung; local proliferation of T$_{VM}$ cells that had arrived in the lung within the first day was tested by Ki67 staining 5 days after infection (Figure 5A). T$_{VM}$ cells typically contained ~20% Ki67$^+$ cycling cells at any moment; this fraction was markedly increased to ~50% in those that arrived in the infected lung during the first day and remained of the T$_{VM}$ phenotype after 5 days (Figure 5B-C). This increase was significantly blunted by intratracheal administration of a blocking antibody against the class I MHC molecule. These data suggest infiltrating T$_{VM}$ cells proliferated locally in an MHC-dependent manner.

Next, we used tetramer staining to trace D^b/NP$_{366-374}$-binding, PR8-specific T$_{VM}$ cells in the infected lung. Given the prevailing frequency of these tetramer-binding cells in the T$_{VM}$ repertoire and the number of infiltrating T$_{VM}$ cells, we estimated there were on average ~10 such T$_{VM}$ cells arriving in the lung in the first day after PR8 infection. Over the next 6 days when FTY720 was given daily to block new entry, the total number of CD44$^+$ D^b/NP$_{366-374}$-binding cells still markedly increased from ~100 at day 3 to ~10^5 at day 7, indicative of substantial proliferation in situ (Figure 5D-E). Importantly, the expanding population included those that assumed a CD62L$^-$CD44$^+$ effector phenotype (Figure 5D, bottom row) and those of a CD62L$^+$CD44$^+$ phenotype (Figure 5D, middle row), which increased from ~40 cells at day 3 to ~3000 cells at day 7 (Figures 5D-E). Among CD62L$^-$CD44$^+$ cells, while some would be descendants of T$_{VM}$ cells that lost CD62L during proliferation, some could have been activated outside the lung and recruited as effector cells after becoming less sensitive to the FTY720 blockade. Conversely, CD62L$^+$CD44$^+$ cells would have to mainly, if not exclusively, come from T$_{VM}$ cells that were recruited into the lung before the start of FTY720 blockade (Figure 5A). To validate this interpretation, we compared FTY720 and PBS treatment (Figure S7A). As expected, total CD8$^+$ T cells in the blood were severely depleted by FTY720 treatment (Figure S7B). Also as expected, significantly fewer D^b/NP$_{366-374}$-binding T cells of a CD62L$^+$CD44$^+$ phenotype were recovered in the FTY720 group (Figure S7C-E), whereas no difference was observed in the draining lymph node (dLN; Figure S7F-H). Therefore, some T$_{VM}$ cells must be able to proliferate in the lung while maintaining the CD62L$^+$CD44$^+$ phenotype, a phenomenon we verified *in vitro* (Figure S7I).

To further rule out the possibility that the expanding population of D^b/$NP_{366-374}$-binding cells that maintained the $CD62L^+CD44^+$ phenotype might have come to the lung only after clonal expansion in the dLN, we compared $\alpha\beta$ TCR sequences recovered from single D^b/$NP_{366-374}$-binding $CD62L^+CD44^+$ T cells in the lungs and the dLN from 4 individual mice. In all 4 mice analyzed, the lungs contained a more diverse group of T cell clones, including uniquely expanded ones (Figure 5F-G); in two of the 4 mice (#3 and #4), we did not detect any shared clones between the lung and the dLN (see Data S1 for all $\alpha\beta$ sequences). For comparison, we also sequenced single D^b/$NP_{366-374}$-binding $CD62L^+CD44^+$ T cells from one control mouse (5#) without FTY720 treatment. In sharp contrast, now all but one expanded clonotype recovered from the lung were found in the dLN (Figure 5H) (see Data S1 for all $\alpha\beta$ sequences). Together, these data demonstrate that T_{VM} cells in the early infiltration contain virus-specific clones, and these cells can be locally retained to expand directly in the lung, with some progenies maintaining a central-memory phenotype.

T_{VM} cells are better poised for T_{RM} development

Local expansion supported by tissue dendritic cells and niche environment (*6, 39*) may be particularly conducive to T_{RM} generation (*2, 7*). To test the possibility that T_{VM} cells may be poised to produce T_{RM} cells, sort-purified polyclonal CD45.2 T_{VM} or naïve T (T_N) cells were transferred into CD45.1 mice that were subsequently infected with the PR8 virus. 21 days after infection, both groups had $CD45.2^+$ $CD8^+$ T cells in their lungs, containing both $CD69^+CD103^-$ and $CD69^+CD103^+$ T_{RM} cells (Figure 6A). Interestingly, there were more lung $CD8^+$ T cells derived from $CD45.2^+$ T_{VM} than from $CD45.2^+$ T_N precursors (Figure 6B), and T_{VM} precursors exhibited a 3- to 5-fold advantage in giving rise to $CD69^+CD103^-$ (Figure 6C) and $CD69^+CD103^+$ (Figure 6D) T_{RM} cells. This is in contrast to the fact that T_{VM} precursors gave rise to fewer LLMP cells in the spleen after infection (Figure 3J-K). To more directly compare T_{VM} and T_N precursors for their abilities to give rise to T_{RM} cells following infection in the same host environment, T_{VM} and T_N cells were sort-purified from either CD45.1 or CD45.2 donor mice, mixed in either of the two possible combinations at a 1:1 ratio, and co-transferred into $Cd8^{-/-}$ recipients that were subsequently infected with PR8. Thirty days after infection, we quantitated contribution by T_{VM} and T_N precursors in the T_{RM} compartment. In a majority of recipients (11/14), donor T_{VM} precursors made dominant (>80%) contribution to the T_{RM} compartment, whereas donor T_N precursors only dominated in 1 of the 14 recipients, regardless of CD45.1/CD45.2 combination used (Figure 6E-F). We also sort-purified $CCR2^+$ T_{VM} cells, $CCR2^-$ T_{VM} cells and T_N cells from $Ccr2^{rfp/+}$ reporter mice and tested their T_{RM}-generating potentials after transfer into $Cd8^{-/-}$ mice. In these studies, the $CCR2^-$ T_{VM} subset produced the highest number of T_{RM} cells (Figure 6G-J). These data demonstrate that T_{VM} cells are not only capable of but more prone to developing into tissue-resident memory, a feature

for which the CCR2$^-$ subset is more responsible. This advantage of T$_{VM}$ cells could stem from the fact that T$_{VM}$ cells are intrinsically able to arrive rapidly and proliferate in the inflamed tissue. On the other hand, a polyclonal T$_{VM}$ cell population probably contains more clonotypes that are more frequently and/or strongly exposed to self antigen in the periphery than a polyclonal T$_N$ cell population. It thus remains possible that self affinities to tissue antigen would confer a certain advantage for T$_{RM}$ generation and maintenance.

To further probe these two potential contributing factors, T$_{VM}$ and T$_N$ cells were sort-purified from either CD45.1 OT-I or CD45.1/2 OT-I donor mice to allow the same OT-I TCR on the two types of cells, mixed in either of the two possible congenic-marker combinations at a 1:1 ratio, and co-transferred into B6 mice that were subsequently infected with the recombinant PR8-OVA virus. To approach a physiological frequency of single TCR clonotypes, we transferred 40 OT-I T$_{VM}$ and 40 OT-I T$_N$ cells to each recipient. Donor T$_{VM}$ OT-I cells made dominant (>80%) contribution to lung T$_{RM}$ cells in 21 of 44 recipients, regardless of CD45.1/CD45.2 combination used, whereas donor T$_N$ OT-I cells made dominant contribution only in 9 of 44 recipients (Figure 6K-L). These data suggest that the intrinsic nature of T$_{VM}$ cells confers an increased ability to generate lung T$_{RM}$ cells in a manner independent of TCR specificities. The occurrence of dominance (>80% contribution by either T$_{VM}$ or T$_N$ precursors) in 30 of 44 OT-I recipients suggests the outcome of lung T$_{RM}$ development by T$_{VM}$ or T$_N$ precursors of the same clonotype is mainly determined at an early stage when their numbers are limiting, consistent with early tissue infiltration and local expansion being an important factor. Notably, however, the T$_{VM}$ advantage observed with the fixed OT-I TCR is smaller than the overall advantage observed with polyclonal T$_{VM}$ cells (Figure 6E-F). The fact that, when a polyclonal pool of specificities and clonotypes are available, dominance is more often achieved by T$_{VM}$ precursors implies that TCR specificities and clonotypes enriched in T$_{VM}$ cells may offer advantages conducive for T$_{RM}$ generation in the lung.

Discussion

Our study identifies two subsets of T$_{VM}$ cells that are phenotypically stable at the steady-state and show a division of labor: a more effector-ready CCR2$^+$ and a more progenitor-poised CCR2$^-$ T$_{VM}$ populations. Given Catnb$_{329-336}$ stimulation of OT-I cells *in vitro* could lead to CCR2 upregulation, a simplistic view is that CCR2$^+$ T$_{VM}$ cells would preferentially develop from T$_{VM}$ with higher affinities for self antigen. However, we have not been able to stimulate CCR2 upregulation on OT-I T cells *in vivo* by injecting up to 1 mg Catnb$_{329-336}$ peptide. In light of the fact that the two subsets do not differ in CD5 expression, additional factors are probably at play. For example, the particular homeostatic cytokine milieu in which a given T cell recognizes its self antigen could be a critical factor for CCR2 upregulation. The abundance of such self antigen and thus the frequency and intensity by which a given T cell sees the self antigen could also be

important. With equal intrinsic affinity, T cells exposed to more antigen may preferentially develop into the CCR2$^+$ subset. We also cannot exclude the possibility that microbiota-derived antigen, albeit not essential, may contribute to generation of CCR2$^+$ T$_{VM}$ cells.

Conversely, when exposed to *bona fide* agonistic foreign antigen, T cells could only upregulate CCR2 at a very low dose of antigen. By extension, there may also be a limit on self antigen exposure beyond which T cells can no longer upregulate CCR2. Besides homeostatic TCR signals (*21*), future studies are warranted to delineate precisely how these other factors may influence phenotypic and functional distinctions between the CCR2$^+$ and CCR2$^-$ subsets.

Upon viral infection, T$_{VM}$ cells can be rapidly recruited to the target tissue and collectively orchestrate an extra-lymphoid primary response. Because they do not overtly express CD49d, other integrins are likely to be involved in early recruitment to the tissue. Notably, T$_{VM}$ cells have been reported to contribute substantially to an immune response to lung infection in aged mice (*40*). At the onset of infection, newly recruited T$_{VM}$ cells likely control viral replication, probably in an antigen non-specific manner. Because virus-specific clones within infiltrating polyclonal T$_{VM}$ cells can then clonally expand in the tissue, T$_{VM}$-derived cells are expected to also participate in antigen-specific control of the virus. Although our results in the model of *Listeria* infection and cytokine production *in vitro* imply CCR2$^+$ T$_{VM}$ cells would play a more dominant role in providing early protection, future studies are necessary to fully elucidate functional distinction between CCR2$^+$ and CCR2$^-$ T$_{VM}$ subsets against flu and other viral infections.

We demonstrated that T$_{VM}$ cells have an increased ability to produce T$_{RM}$ cells and, in this regard, CCR2$^-$ T$_{VM}$ cells play a more dominant role. This increased T$_{RM}$-generating ability is reminiscent of previous findings that T$_{VM}$ precursors would proliferate more than their naïve counterparts and can generate more T$_{CM}$ cells than their true memory counterparts (*19*). As an interesting correlate, T$_{VM}$ cells express relatively uniformly CXCR5, which is associated with stemness in CD8$^+$ T cells during chronic infections and cancer (*23-25*). The rapid recruitment and early tissue entrapment probably subject antigen-specific T$_{VM}$ cells to prolonged exposure to residence-inducing factors such as TGF-β (*41, 42*), thus favoring T$_{RM}$ development. In contrast, naïve antigen-specific precursors are trapped in secondary lymphoid organs (SLOs) to expand before acquiring the ability to migrate into the target tissue, even though TGF-β in SLOs may directly condition a fraction of naïve T cells for an increased propensity to develop into T$_{RM}$ cells during the subsequent response to infection (*43*). In our work, the observed advantage of T$_{VM}$ precursors implies that the tissue niche for T$_{RM}$ generation and maintenance may be limited in size (*6, 44*), thus discriminating against late-arriving cells. It is not clear how TCR clonotypes of the T$_{VM}$ population may favor T$_{RM}$ generation in the lung. A provocative possibility is that self antigen recognition may contribute to T$_{RM}$ generation

and maintenance, and consequently the virus-specific T_{RM} compartment might prefer those that have higher affinities for self antigen present in the lung. The fact that T_{VM} cells can orchestrate an extra-lymphoid primary response, to execute early viral control on the one hand and to produce T_{RM} cells locally on the other, suggests yet another way by which the immune system harnesses unavoidable self affinities to better fight microbial invasions (*22, 45*). Selective deployment of virus-specific T_{VM} cells in the lung might be a strategy to design T_{RM}-based prophylactic vaccines for pulmonary infections.

Materials and Methods

Study design

The aim of this study was to investigate the role of virtual memory T cells in primary tissue immune response towards pathogen infection. Heterogeneous subsets of T_{VM} cells were defined with CCR2 expression. Functional properties of CCR2$^+$ and CCR2$^-$ T_{VM} cells were characterized with *in vitro* and *in vivo* stimulation with antigen or inflammatory cytokine derived signals. Antiviral or antibacterial protections of T_{VM} cells were assessed with adoptive transfer of T cells subsets or mixed-bone marrow chimera assay. Local proliferation of T_{VM} cells in tissue was characterized and quantified with antibody blocking, tetramer specific cell staining and single cell TCR sequencing. Derivation of T_{RM} cells from T_{VM} or T_N cells was assessed with adoptive cell transfer. Control and experimental treatments or divisions were administered randomly with sex- and age-matched mice. Mice and replicates of the experiments were presented in the figure legends.

Mice

B6 (Jax 664), CD45.1 (Jax 2014), OT-I (Jax 3831), *Cd8$^{-/-}$* (Jax 2665), *Cxcr3$^{-/-}$* (Jax 5796) *Ccr2$^{rfp/rfp}$* (Jax 17586), IRES-YFP IFN-γ reporter strain (Jax 1758), Nur77-GFP (Jax 16617) were originally from the Jackson Laboratory. Age-matched littermates between 6 and 12 weeks of age were used for experiments. Sample sizes for mouse experiments were empirically determined, and mice were randomly assigned to control or experimental group. No blinding was necessary for mouse experiments presented in this study. All mice were maintained under specific-pathogen free conditions, with experimental protocols approved by the Tsinghua Institutional Animal Care and Use Committee.

Bone marrow chimera

Bone marrow cells of indicated genotypes were isolated, mixed at indicated ratios, and transferred (a total of 2×10^6 cells per recipient) into lethally irradiated (5.5 Gy $\times$2) B6 mice (for CD45.1:CD45.2 *Ccr2$^{+/+}$* and CD45.1:CD45.2 *Ccr2$^{rfp/rfp}$* chimera) or *Cd8$^{-/-}$* recipients (for *Cxcr3$^{+/y}$:Cd8$^{-/-}$* and *Cxcr3$^{-/y}$:Cd8$^{-/-}$* chimera). Chimeric mice were given

antibiotics in drinking water (1 mg/ml neomycin and 100 ng/ml polymyxin, Inalco Pharmaceuticals) for 4 weeks and used 8 weeks after reconstitution.

Viruses, bacteria and infection

Influenza H1N1 PR8, PR8-OVA strain was propagated in embryonated hen eggs from virus stocks. For influenza infection, depending on experimental purposes, mice were intranasally infected with 20 to 10^4 PFU PR8, 100 PFU PR8-OVA under mild anesthesia by intraperitoneal tribromoethanol (250 mg/kg). Recombinant *L. monocytogenes* strain expressing ovalbumin protein (*Lm*-OVA) was grown in brain heart infusion medium with 50 µg/ml streptomycin to an OD600 of ~0.1. For testing CCR2$^+$ T$_{VM}$-, CCR2$^-$ T$_{VM}$- and T$_N$-mediated protection, *Cd8*$^{-/-}$ recipient mice were intravenously infected with a lethal dose of 10^5 CFU *Lm*-OVA. For testing responses of OT-I CCR2$^+$ T$_{VM}$, CCR2$^-$ T$_{VM}$ and T$_N$ cells to *Lm*-OVA, mice were intravenously infected with 10^4 CFU of the bacteria.

Adoptive transfer

For assays involving adoptive transfer of primary CD8 T cells, total splenic CD8 T cells were isolated using the CD8 T cell isolation kit (Miltenyi Biotec) according to the manufacturer's protocol. After staining with fluorescein conjugated antibodies, CD44$^+$CD62L$^+$ T$_{VM}$ cells, CD44$^-$CD62L$^+$ T$_N$ cells, CCR2$^+$ or CCR2$^-$ CD44$^+$CD62L$^+$ T$_{VM}$ cells from B6, *Ccr2*$^{rfp/+}$, OT-I, *Ccr2*$^{rfp/+}$ OT-I mice were sort-purified with >90% purity and transferred into recipients at indicated cell numbers. Indicated combinations of CD45.1, CD45.2, or CD45.1/2 were used in co-transfer to distinguish different donor populations in the same recipients. For testing generation of CCR2$^+$ T$_{VM}$ cells from homeostatic proliferation of naïve T cells, 10^6 freshly isolated naïve CD8 T cells from *Ccr2*$^{rfp/+}$ mice were transferred into sublethally irradiated (5.5 Gy) CD45.1 recipients, which were analyzed 3 weeks later. For testing generation of CCR2$^+$ T$_{VM}$ cells by naïve OT-I T cells during homeostatic proliferation, 3×10^5 freshly isolated naïve CD8 T cells from CD45.1 *Ccr2*$^{rfp/+}$ OT-I mice were transferred into sublethally irradiated (5.5 Gy) B6 recipients, which were then analyzed 3 weeks later.

Antibody and drug treatment of mice

To block lymphocyte egress from lymphoid organs, mice were intraperitoneally treated with 1mg/kg Fingolimod (FTY720) (Selleck) or PBS daily from the second day after infection until being sacrificed. To block antigen-dependent proliferation of CD8 T cells in the lung, mice were intratracheally given 200 µg anti-MHC class I antibody (H-2) (M1/42.3.9.8, Bioxcell) in 50 µl PBS under mild anesthesia by intraperitoneal tribromoethanol (250 mg/kg).

Cell culture and *in vitro* stimulation

To test CCR2 expression *in vitro*, splenic CD8 T cells from $Ccr2^{rfp/+}$ OT-I mice were isolated using the CD8 T cell isolation kit (Miltenyi Biotec) according to the manufacturer's protocol. $CD44^-CD62L^+$ naïve OT-I T cells were then sort-purified and stimulated with $OVA_{257-264}$ or $Catnb_{329-336}$ peptide at indicated final concentrations in the presence of 8 ng/ml IL-2 and splenocytes that were pre-treated with mitomycin (50 µg/ml, Sigma). When indicated, IL-7 and IL-15 were used at a final concentration of 20 ng/ml. To test cytokine-stimulated IFN-γ production, $CCR2^+$ and $CCR2^-$ T_{VM} cells were sort-purified from $Ccr2^{rfp/+}$ mice and stimulated for 16 h with 10 ng/ml IL-12, 10 ng/ml IL-18, and 10U/ml IL-2 and for the last 4 h in the presence of GolgiPlug (BD Biosciences). Cells were fixed and permeabilized with Cytofix/Cytoperm Fixation/Permeabilization Solution Kit from BD Biosciences and then intracellularly stained with anti-IFN-γ (XMG1.2). To test TCR-dependent activation, sort-purified $CCR2^+$ and $CCR2^-$ T_{VM} cells from $Ccr2^{rfp/+}$ mice were stimulated for 4 h with indicated concentrations (0.1-1 µg/ml) of plate-bound anti-CD3 together with 10 µg/ml anti-CD28 and GolgiPlug (BD Biosciences). Cells were then stained with anti-CD25 (PC61) and anti-CD69 (H1.2F3) before subjected to intracellularly staining for IFN-γ as above.

Quantification of the *Lm*-OVA bacterial load in tissues

Four days after *Lm*-OVA infection, spleens and livers from infected mice were removed, weighted, and then homogenized in cold PBS containing 0.5% Triton (Sigma). Serial dilutions of tissue homogenates were plated and cultured at 37°C in brain heart infusion (Solarbio) plate containing 50 mg/ml streptomycin. Bacterial colonies were counted after 24 h, as previously described (*46*).

Lung-infiltrating lymphocytes

To distinguish tissue-infiltrating cells from cells in the blood compartment, mice were intravenously injected with 2 µg of fluorochrome-conjugated anti-CD45.1 (clone A20) or anti-CD45.2 (clone 104) antibody 3 minutes before being sacrificed. The lung tissue was enzymatically digested in RPMI medium containing 20 µg/ml DNase I (Roche) and 40 µg/ml Liberase CI (Roche) at 37°C for 30 minutes. Tissue digest was then subjected to Percoll density-gradient centrifugation (40%/70%) at 1300 *g* for 30 minutes. Cells at the gradient interface were collected for downstream flow-cytometric analyses, and cells pre-labeled with intravenously injected antibodies were excluded by gating.

Flow cytometry

Cells from lung or secondary lymphoid organs were harvested, washed and incubated with 20 µg/ml 2.4G2, and then stained with indicated monoclonal antibodies in MACS buffer (PBS containing 1% FBS and 5 mM EDTA). Primary staining reagents included ef450 anti-CD3 (145-2C11), FITC anti-CD3 (145-2C11), Alexa Fluor 700 anti-CD44 (IM7), ef450 anti-CD45.1 (A20), FITC anti-CD11a (M17/4) from eBioscience; APC-Cy7

anti-CD8a (53-6.7), APC-Cy7 anti-CD8b (YTS156.7.7), FITC anti-CD5 (53-7.3), BV421 anti-CD25 (PC61), PE-Cy7 anti-CD44 (IM7), PE-Cy7 anti-CD69 (H1.2F3), BV421 anti-IFN-γ (XMG1.2), Alexa Fluor 647 anti-Ki67 (B56) from BD Biosciences; APC anti-CD8a (53-6.7), FITC anti-CD45.1 (A20), Pacific Blue or FITC anti-CD45.2 (104),

APC anti-CD62L (MEL-14), APC anti-CD122 (TM-β1), BV510 anti-CD103 (2E7),

BV421 anti-CXCR3 (CXCR3-173), Biotin anti-CCR5 (HM-CCR5), Streptavidin-PE (405207) from BioLegend, Biotin anti-CXCR5 (REA215) from Miltenyi Biotec, Alexa Fluor 647 Goat anti-Rat IgG H&L from Abcam, Rabbit anti-RFP (600-401-379) from Rockland, 7-amino-actinomycin D (7-AAD) from Biotium. Isotype-matched control antibodies were purchased from the same companies. T-select-H-2D^b-Influenza NP tetramer-ASNENMETM-APC and H-2D^b-Influenza PA tetramer- SSLENFRAYV-APC were purchased from MBL. For intracellular staining of cytokines, the Cytofix/Cytoperm Fixation/Permeabilization Solution Kit from BD Biosciences was used. To measure cell division by dye dilution, the CellTrace CFSE Cell Proliferation Kit (Thermo Fisher) was used. Cells were stained on ice with primary antibodies for 30-90 min followed by staining with secondary antibodies for 30 min. Data were collected on LSRII cytometer (BD Biosciences). For analyzing TCR β chain usage, Anti-Mouse TCR Vβ Screening Panel (BD Biosciences) kit was used. For sorting, indicated cell populations were sorted to >90% purity with Aria III cytometer (BD Biosciences). Non-singlets were excluded from analysis based on the forward scatter height (FSC-H), forward scatter width (FSC-W), side scatter height (SSC-H) and side scatter width (SSC-W) characteristics.

Enrichment of tetramer-binding cells.
H-2D^b-NP$_{366-374}$- and H-2D^b-PA$_{224-233}$-binding cells from naïve B6 mice were enriched using a previously described protocol (*12*). Briefly, splenocytes from SPF B6 mice (6-8 weeks of age) were harvested, washed and incubated with 30 μl T-select-H-2D^b-Influenza NP tetramer-ASNENMETM-APC or H-2D^b-Influenza PA tetramer- SSLENFRAYV-APC, in 300 μl staining buffer (150 μl 2.4G2 supernatant, 150 μl HBSS containing 2% FCS and 0.2% azide) at 4°C for 60 minutes. Cells were then washed, resuspended in staining buffer, and stained with anti-APC-coupled MACS Microbeads (Miltenyi Biotec) for 30 minutes at 4°C. Cells were then washed and tetramer-binding cells were isolated with MACS columns (Miltenyi Biotec) according to manufacturer's instructions. After elution, cells were washed and resuspended in MACS buffer and stained for indicated markers (CD8, CD44, CD122, and CCR2).

Disease course and viral load measurement
Individual mice were weighted daily before and after PR8 infection until day 5. Following euthanasia, lungs were removed, weighted and homogenized in Trizol (Thermo Scientific) for RNA extraction. Extracted RNA was reverse transcribed with

IAV *segment 7 matrix protein 2* primer (5'-CATCCTGTTGTATATGAGGCCCAT-3')
and Oligo dT using RevertAid Minus First Strand cDNA synthesis Kit (Thermo
Scientific). Real-time PCR was performed with RealStar Green Power Mixture
(Genestar). The viral titer is standardized with known quantity of PR8 virus stock. IAV
segment 7 matrix protein 2 primers for real-time PCR are: forward-5'-
GGACTGCAGCGTAGACGCTT-3', reverse-5'-
CATCCTGTTGTATATGAGGCCCAT3'.

Chemokine receptor screening by RT-PCR
RNA was extracted from sort-purified cells with Rneasy Plus Mini Kit (Qiagen) and was
reverse-transcribed with RevertAid Minus First Strand cDNA synthesis Kit (Thermo
Scientific). Real-time PCR was performed with RealStar Green Power Mixture (Genestar)
on a 7500 Realtime PCR system (ABI). Primers used were listed in Table S4.

RNA-seq analyses
For bulk RNA-seq of $CCR2^+$ T_{VM} and $CCR2^-$ T_{VM} cells, a previously used protocol that is
suitable for 200 sorted lymphocytes was used(*47*). All libraries were prepared with
Illumina TrueSeq sequencing kit and were sequenced on a HiSeq 2500 sequencer
(Illumina) in SE-50 mode in Tsinghua University. The raw data were processed with
CASAVA (Illumina) for generating fastq files, followed by aligning reads to the *Mus
musculus* reference genome with TopHat2 and assembling Cufflinks to calculate the
FPKM for each transcript. Differential expression between cell subsets was calculated by
DESeq2 (Bioconductor) with a threshold of adjusted $p_{adj}<0.05$. A total of 3 independent
experiments were conducted, and for each experiment 4 mice per group were pooled for
sorting desired cell populations. Two to 4 independent sorts of each cell type per
experiment were harvested.

Single-cell TCR clonotype analyses
Tetramer-binding $CD8^+$ T cells were sorted from the lung-infiltrating cell preparation or
the draining lymph node of the same mouse. Single sorted cells were directly lysed in
0.2% Trion containing RNase inhibitor (Takara). Total cDNA from a single cell was
reverse-transcribed, and cDNA was pre-amplified using the Smart-seq2 protocol(*48*) .
Sequences of α and β chains were amplified and sequenced using a nested PCR strategy
by combining mouse TCR-specific primers as described in(*49*) and the plate-barcoding
strategy as described in (*50*). The specific set of primers and barcodes used here is
provided in the spreadsheet format in Data S2. Briefly, in the first-round PCR, ~3ng in
1µl cDNA was used to amplify TCR α and β sequences separately using HotStarTaq
DNA polymerase (Qiagen) by manufacturer's instructions in a 20-µl reaction. Primers for
Vα, Vβ, Cα and Cβ were diluted and mixed so that the final concentration was 0.06 µM
for each V primer and 0.3 µM for each C primer. The cycling condition was: 95°C 5 min;

95°C 30 s, 56°C 30 s, 72 °C 1 min, ×18 runs; 72 °C 10 min; 12 °C. In the second-round, 1 μl product from the 1st-round reaction was used as template to amply by the same cycling parameters and primer concentrations. The primers used for the 2nd-round PCR reaction were internally nested in the amplicons resulting from the 1st reaction but those V primers contained a 23-base PCR handle sequence(50) at the 5' end for subsequent amplification. The third-round PCR was performed using 1 μl product of the 2nd-round PCR as the template and barcoding primers (0.5 μM) that permit indexing cells in the 96-well format. The forward primer set contains the complementary sequence to the PCR handle introduced in the 2nd round, an anchor sequence for Illumina paired-end sequencing, and a barcode in the middle to index the row. The reverse primer set contains sequence complementary to Cα or Cβ, another anchor sequence for paired-end sequencing, and a barcode in the middle to index the column. The cycling condition was the same as above except for only 8 runs. After that, Illumina Paired-End primers (0.5 μM each) were used to amply for 8 more cycles to prepare for sequencing. The final PCR product was cleaned using vazyme clean beads individually, and products corresponding to TCR α and β chains from individual cells were mixed and sequenced (paired-end, 150-bp) on Illumina HiSeq Xten platform. Combinational cell barcodes were used to filter out invalid cells. TCR sequences were analyzed by IGBLAST. Paired-end sequencing at the 150-bp depth was sufficient for covering the CDR3 to permit clonotype analyses, although it did not allow reconstruction of the entire V sequence so that mapping to more than one V genes in the same family was common.

References:

1. J. T. Harty, V. P. Badovinac, Shaping and reshaping CD8+ T-cell memory. *Nat Rev Immunol* **8**, 107-119 (2008).
2. S. C. Jameson, D. Masopust, Understanding Subset Diversity in T Cell Memory. *Immunity* **48**, 214-226 (2018).
3. T. Gebhardt, L. M. Wakim, L. Eidsmo, P. C. Reading, W. R. Heath, F. R. Carbone, Memory T cells in nonlymphoid tissue that provide enhanced local immunity during infection with herpes simplex virus. *Nat Immunol* **10**, 524-530 (2009).
4. D. Masopust, D. Choo, V. Vezys, E. J. Wherry, J. Duraiswamy, R. Akondy, J. Wang, K. A. Casey, D. L. Barber, K. S. Kawamura, K. A. Fraser, R. J. Webby, V. Brinkmann, E. C. Butcher, K. A. Newell, R. Ahmed, Dynamic T cell migration program provides resident memory within intestinal epithelium. *J Exp Med* **207**, 553-564 (2010).
5. S. Ariotti, J. B. Beltman, G. Chodaczek, M. E. Hoekstra, A. E. van Beek, R. Gomez-Eerland, L. Ritsma, J. van Rheenen, A. F. Maree, T. Zal, R. J. de Boer, J. B. Haanen, T. N. Schumacher, Tissue-resident memory CD8+ T cells continuously patrol skin epithelia to quickly recognize local antigen. *Proc Natl Acad Sci U S A* **109**, 19739-19744 (2012).
6. D. L. Turner, K. L. Bickham, J. J. Thome, C. Y. Kim, F. D'Ovidio, E. J. Wherry, D. L. Farber, Lung niches for the generation and maintenance of tissue-resident memory T cells. *Mucosal Immunol* **7**, 501-510 (2014).
7. S. N. Mueller, L. K. Mackay, Tissue-resident memory T cells: local specialists in immune defence. *Nat Rev Immunol* **16**, 79-89 (2016).
8. M. A. Weinreich, O. A. Odumade, S. C. Jameson, K. A. Hogquist, T cells expressing the transcription factor PLZF regulate the development of memory-like CD8+ T cells. *Nat Immunol* **11**, 709-716 (2010).
9. R. Horai, K. L. Mueller, R. A. Handon, J. L. Cannons, S. M. Anderson, M. R. Kirby, P. L. Schwartzberg, Requirements for selection of conventional and innate T lymphocyte lineages. *Immunity* **27**, 775-785 (2007).
10. L. O. Atherly, J. A. Lucas, M. Felices, C. C. Yin, S. L. Reiner, L. J. Berg, The Tec family tyrosine kinases Itk and Rlk regulate the development of conventional CD8+ T cells. *Immunity* **25**, 79-91 (2006).
11. C. Broussard, C. Fleischacker, R. Horai, M. Chetana, A. M. Venegas, L. L. Sharp, S. M. Hedrick, B. J. Fowlkes, P. L. Schwartzberg, Altered development of CD8+ T cell lineages in mice deficient for the Tec kinases Itk and Rlk. *Immunity* **25**, 93-104 (2006).
12. C. Haluszczak, A. D. Akue, S. E. Hamilton, L. D. Johnson, L. Pujanauski, L. Teodorovic, S. C. Jameson, R. M. Kedl, The antigen-specific CD8+ T cell

repertoire in unimmunized mice includes memory phenotype cells bearing markers of homeostatic expansion. *J Exp Med* **206**, 435-448 (2009).

13.   A. D. Akue, J. Y. Lee, S. C. Jameson, Derivation and maintenance of virtual memory CD8 T cells. *J Immunol* **188**, 2516-2523 (2012).

14.   J. T. White, E. W. Cross, M. A. Burchill, T. Danhorn, M. D. McCarter, H. R. Rosen, B. O'Connor, R. M. Kedl, Virtual memory T cells develop and mediate bystander protective immunity in an IL-15-dependent manner. *Nat Commun* **7**, 11291 (2016).

15.   B. C. Chiu, B. E. Martin, V. R. Stolberg, S. W. Chensue, Cutting edge: Central memory CD8 T cells in aged mice are virtual memory cells. *J Immunol* **191**, 5793-5796 (2013).

16.   J. T. White, E. W. Cross, R. M. Kedl, Antigen-inexperienced memory CD8(+) T cells: where they come from and why we need them. *Nat Rev Immunol* **17**, 391-400 (2017).

17.   T. Sosinowski, J. T. White, E. W. Cross, C. Haluszczak, P. Marrack, L. Gapin, R. M. Kedl, CD8alpha+ dendritic cell trans presentation of IL-15 to naive CD8+ T cells produces antigen-inexperienced T cells in the periphery with memory phenotype and function. *J Immunol* **190**, 1936-1947 (2013).

18.   V. Martinet, S. Tonon, D. Torres, A. Azouz, M. Nguyen, A. Kohler, V. Flamand, C. A. Mao, W. H. Klein, O. Leo, S. Goriely, Type I interferons regulate eomesodermin expression and the development of unconventional memory CD8(+) T cells. *Nat Commun* **6**, 7089 (2015).

19.   J. Y. Lee, S. E. Hamilton, A. D. Akue, K. A. Hogquist, S. C. Jameson, Virtual memory CD8 T cells display unique functional properties. *Proc Natl Acad Sci U S A* **110**, 13498-13503 (2013).

20.   S. C. Jameson, Y. J. Lee, K. A. Hogquist, Innate memory T cells. *Adv Immunol* **126**, 173-213 (2015).

21.   A. Drobek, A. Moudra, D. Mueller, M. Huranova, V. Horkova, M. Pribikova, R. Ivanek, S. Oberle, D. Zehn, K. D. McCoy, P. Draber, O. Stepanek, Strong homeostatic TCR signals induce formation of self-tolerant virtual memory CD8 T cells. *EMBO J* **37**,   (2018).

22.   R. B. Fulton, S. E. Hamilton, Y. Xing, J. A. Best, A. W. Goldrath, K. A. Hogquist, S. C. Jameson, The TCR's sensitivity to self peptide-MHC dictates the ability of naive CD8(+) T cells to respond to foreign antigens. *Nat Immunol* **16**, 107-117 (2015).

23.   R. He, S. Hou, C. Liu, A. Zhang, Q. Bai, M. Han, Y. Yang, G. Wei, T. Shen, X. Yang, L. Xu, X. Chen, Y. Hao, P. Wang, C. Zhu, J. Ou, H. Liang, T. Ni, X. Zhang, X. Zhou, K. Deng, Y. Chen, Y. Luo, J. Xu, H. Qi, Y. Wu, L. Ye, Follicular CXCR5- expressing CD8(+) T cells curtail chronic viral infection. *Nature* **537**, 412-428 (2016).

24. S. J. Im, M. Hashimoto, M. Y. Gerner, J. Lee, H. T. Kissick, M. C. Burger, Q. Shan, J. S. Hale, J. Lee, T. H. Nasti, A. H. Sharpe, G. J. Freeman, R. N. Germain, H. I. Nakaya, H. H. Xue, R. Ahmed, Defining CD8+ T cells that provide the proliferative burst after PD-1 therapy. *Nature* **537**, 417-421 (2016).

25. Y. A. Leong, Y. Chen, H. S. Ong, D. Wu, K. Man, C. Deleage, M. Minnich, B. J. Meckiff, Y. Wei, Z. Hou, D. Zotos, K. A. Fenix, A. Atnerkar, S. Preston, J. G. Chipman, G. J. Beilman, C. C. Allison, L. Sun, P. Wang, J. Xu, J. G. Toe, H. K. Lu, Y. Tao, U. Palendira, A. L. Dent, A. L. Landay, M. Pellegrini, I. Comerford, S. R. McColl, T. W. Schacker, H. M. Long, J. D. Estes, M. Busslinger, G. T. Belz, S. R. Lewin, A. Kallies, D. Yu, CXCR5(+) follicular cytotoxic T cells control viral infection in B cell follicles. *Nat Immunol* **17**, 1187-1196 (2016).

26. M. Hashimoto, A. O. Kamphorst, S. J. Im, H. T. Kissick, R. N. Pillai, S. S. Ramalingam, K. Araki, R. Ahmed, CD8 T Cell Exhaustion in Chronic Infection and Cancer: Opportunities for Interventions. *Annu Rev Med* **69**, 301-318 (2018).

27. S. L. Deshmane, S. Kremlev, S. Amini, B. E. Sawaya, Monocyte chemoattractant protein-1 (MCP-1): an overview. *J Interferon Cytokine Res* **29**, 313-326 (2009).

28. N. Saederup, A. E. Cardona, K. Croft, M. Mizutani, A. C. Cotleur, C. L. Tsou, R. M. Ransohoff, I. F. Charo, Selective chemokine receptor usage by central nervous system myeloid cells in CCR2-red fluorescent protein knock-in mice. *PLoS One* **5**, e13693 (2010).

29. F. R. Santori, W. C. Kieper, S. M. Brown, Y. Lu, T. A. Neubert, K. L. Johnson, S. Naylor, S. Vukmanovic, K. A. Hogquist, S. C. Jameson, Rare, structurally homologous self-peptides promote thymocyte positive selection. *Immunity* **17**, 131-142 (2002).

30. A. Tarakhovsky, S. B. Kanner, J. Hombach, J. A. Ledbetter, W. Muller, N. Killeen, K. Rajewsky, A role for CD5 in TCR-mediated signal transduction and thymocyte selection. *Science* **269**, 535-537 (1995).

31. H. S. Azzam, A. Grinberg, K. Lui, H. Shen, E. W. Shores, P. E. Love, CD5 expression is developmentally regulated by T cell receptor (TCR) signals and TCR avidity. *J Exp Med* **188**, 2301-2311 (1998).

32. K. Takada, S. C. Jameson, Self-class I MHC molecules support survival of naive CD8 T cells, but depress their functional sensitivity through regulation of CD8 expression levels. *J Exp Med* **206**, 2253-2269 (2009).

33. S. P. Persaud, C. R. Parker, W. L. Lo, K. S. Weber, P. M. Allen, Intrinsic CD4+ T cell sensitivity and response to a pathogen are set and sustained by avidity for thymic and peripheral complexes of self peptide and MHC. *Nat Immunol* **15**, 266-274 (2014).

34. R. E. Berg, E. Crossley, S. Murray, J. Forman, Memory CD8+ T cells provide innate immune protection against Listeria monocytogenes in the absence of cognate antigen. *J Exp Med* **198**, 1583-1593 (2003).

35.   T. Kambayashi, E. Assarsson, A. E. Lukacher, H. G. Ljunggren, P. E. Jensen, Memory CD8+ T cells provide an early source of IFN-gamma. *J Immunol* **170**, 2399-2408 (2003).

36.   R. E. Berg, J. Forman, The role of CD8 T cells in innate immunity and in antigen non-specific protection. *Curr Opin Immunol* **18**, 338-343 (2006).

37.   E. Teixeiro, M. A. Daniels, S. E. Hamilton, A. G. Schrum, R. Bragado, S. C. Jameson, E. Palmer, Different T cell receptor signals determine CD8+ memory versus effector development. *Science* **323**, 502-505 (2009).

38.   B. Slutter, L. L. Pewe, S. M. Kaech, J. T. Harty, Lung airway-surveilling CXCR3(hi) memory CD8(+) T cells are critical for protection against influenza A virus. *Immunity* **39**, 939-948 (2013).

39.   S. L. Ng, Y. J. Teo, Y. A. Setiagani, K. Karjalainen, C. Ruedl, Type 1 Conventional CD103(+) Dendritic Cells Control Effector CD8(+) T Cell Migration, Survival, and Memory Responses During Influenza Infection. *Front Immunol* **9**, 3043 (2018).

40.   K. G. Lanzer, T. Cookenham, W. W. Reiley, M. A. Blackman, Virtual memory cells make a major contribution to the response of aged influenza-naive mice to influenza virus infection. *Immun Ageing* **15**, 17 (2018).

41.   L. K. Mackay, A. Rahimpour, J. Z. Ma, N. Collins, A. T. Stock, M. L. Hafon, J. Vega-Ramos, P. Lauzurica, S. N. Mueller, T. Stefanovic, D. C. Tscharke, W. R. Heath, M. Inouye, F. R. Carbone, T. Gebhardt, The developmental pathway for CD103(+)CD8+ tissue-resident memory T cells of skin. *Nat Immunol* **14**, 1294-1301 (2013).

42.   J. M. Schenkel, D. Masopust, Tissue-resident memory T cells. *Immunity* **41**, 886-897 (2014).

43.   V. Mani, S. K. Bromley, T. Aijo, R. Mora-Buch, E. Carrizosa, R. D. Warner, M. Hamze, D. R. Sen, A. Y. Chasse, A. Lorant, J. W. Griffith, R. A. Rahimi, C. P. McEntee, K. L. Jeffrey, F. Marangoni, M. A. Travis, A. Lacy-Hulbert, A. D. Luster, T. R. Mempel, Migratory DCs activate TGF-beta to precondition naive CD8(+) T cells for tissue-resident memory fate. *Science* **366**,   (2019).

44.   S. Takamura, H. Yagi, Y. Hakata, C. Motozono, S. R. McMaster, T. Masumoto, M. Fujisawa, T. Chikaishi, J. Komeda, J. Itoh, M. Umemura, A. Kyusai, M. Tomura, T. Nakayama, D. L. Woodland, J. E. Kohlmeier, M. Miyazawa, Specific niches for lung-resident memory CD8+ T cells at the site of tissue regeneration enable CD69-independent maintenance. *J Exp Med* **213**, 3057-3073 (2016).

45.   K. A. Hogquist, S. C. Jameson, The self-obsession of T cells: how TCR signaling thresholds affect fate 'decisions' and effector function. *Nat Immunol* **15**, 815-823 (2014).

46. S. E. Hamilton, M. C. Wolkers, S. P. Schoenberger, S. C. Jameson, The generation of protective memory-like CD8+ T cells during homeostatic proliferation requires CD4+ T cells. *Nat Immunol* **7**, 475-481 (2006).

47. Y. Wang, J. Shi, J. Yan, Z. Xiao, X. Hou, P. Lu, S. Hou, T. Mao, W. Liu, Y. Ma, L. Zhang, X. Yang, H. Qi, Germinal-center development of memory B cells driven by IL-9 from follicular helper T cells. *Nat Immunol* **18**, 921-930 (2017).

48. S. Picelli, O. R. Faridani, Å. K. Björklund, G. Winberg, S. Sagasser, R. Sandberg, Full-length RNA-seq from single cells using Smart-seq2. *Nature protocols* **9**, 171 (2014).

49. P. Dash, J. L. McClaren, T. H. Oguin, W. Rothwell, B. Todd, M. Y. Morris, J. Becksfort, C. Reynolds, S. A. Brown, P. C. Doherty, Paired analysis of TCRα and TCRβ chains at the single-cell level in mice. *The Journal of clinical investigation* **121**, 288-295 (2011).

50. A. Han, J. Glanville, L. Hansmann, M. M. Davis, Linking T-cell receptor sequence to functional phenotype at the single-cell level. *Nature biotechnology* **32**, 684 (2014).

Author contributions: S.H. and T.S. conducted a majority of the experiments and designed parts of the study. T.M. and J.S. helped with RNA-seq and data analyses, and J.S. helped with TCR cloning. M.M. under the supervision of X.T. produced viruses. H.Q. conceptualized the study, supervised the work, and wrote the paper with S.H. and T.S.

Competing interests: Authors declare no competing interests.

Data and materials availability: RNA-seq data is deposited in GEO under accession number GSE148364. All other data needed to evaluate the conclusions in the paper are present in the paper or the Supplementary Materials.

Supplementary Materials:

Materials and Methods

Figures S1-S7
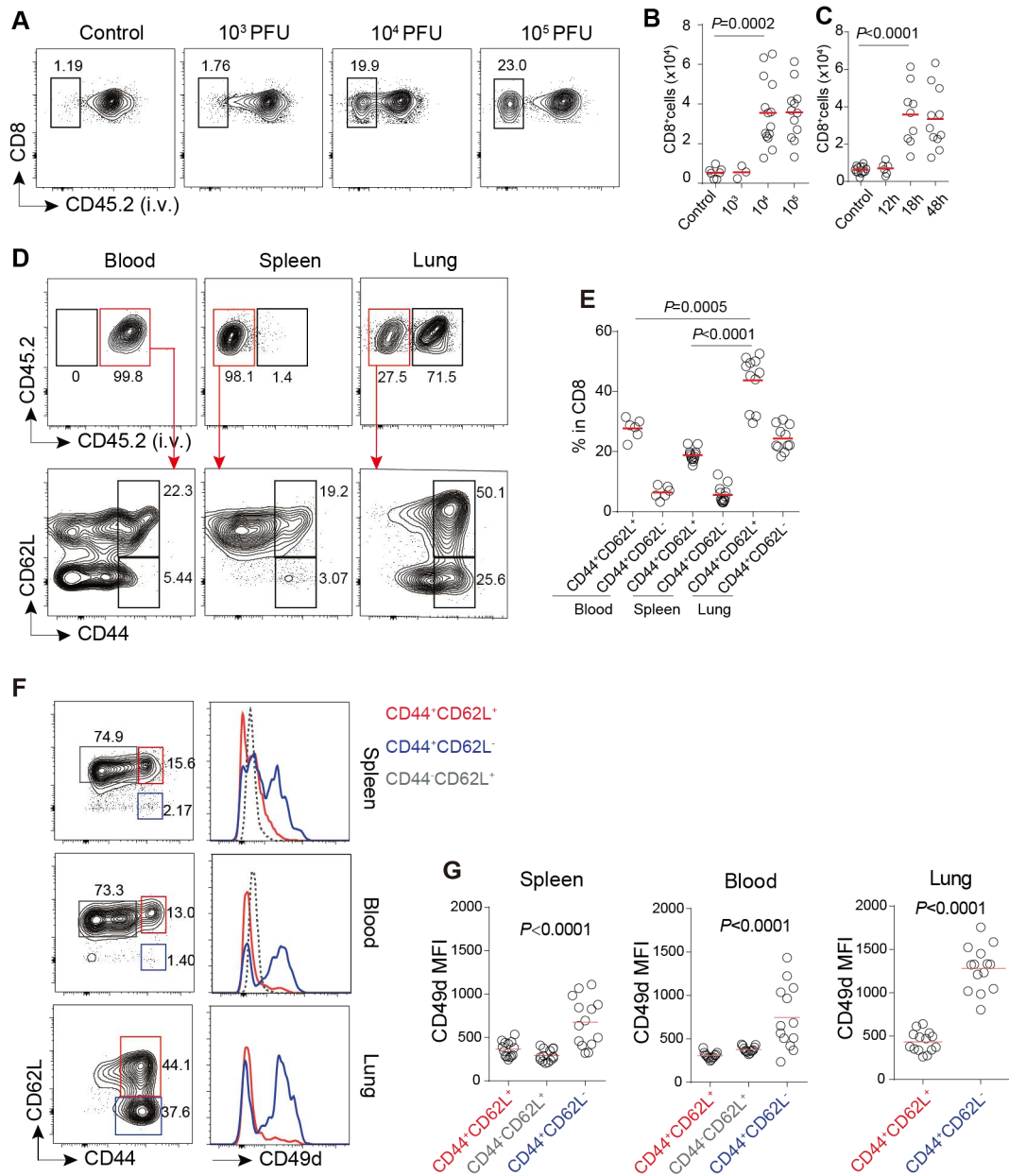
Table S1

Table S2

Table S3

Table S4

Figure 1

Figure 1. Virtual memory T cells rapidly infiltrate flu-infected lung.

(**A**) Representative contour plots of lung-infiltrating CD8^{+} T cells (gated as those negative for staining with 2 μg intravenous anti-CD45.2 3 min before sacrifice) in uninfected control mice or mice infected with indicated doses of influenza PR8 virus 18 h earlier. (**B**) Numbers of infiltrating CD8^{+} T cells after different doses of infection as in (A). (**C**) Numbers of infiltrating CD8^{+} T cells at indicated time points after 10^4 PFU infection as in (A). (**D**) Representative contour plots of blood, splenic and lung CD8^{+} T

cells 1 day after PR8 infection. Top, intravenous CD45 staining; bottom, CD62-CD44 profiles of cells in red gates in the top row. (**E**) Quantitation of $CD62L^+CD44^+$ and $CD62L^-CD44^+$ cells as a percentage of blood, splenic, and lung-infiltrating $CD8^+$ T cells, as in (D). (**F, G**) Representative profiles (F) and summary quantitation (G) of CD49d expression on T cells of $CD62L^+CD44^-$ (gate and histogram in grey), $CD62L^+CD44^+$ (gate and histogram in red), and $CD62L^-CD44^+$ (gate and histogram in blue) phenotype from the spleen, blood and lung (gated on CD45 i.v.$^-$ cells) 1 day after flu infection. In all scatter plots, one dot represents one mouse, and lines denote means; data were pooled from 3 independent experiments; *P* values by one-way ANOVA in spleen and blood. *P* values by unpaired *t* tests in lung.
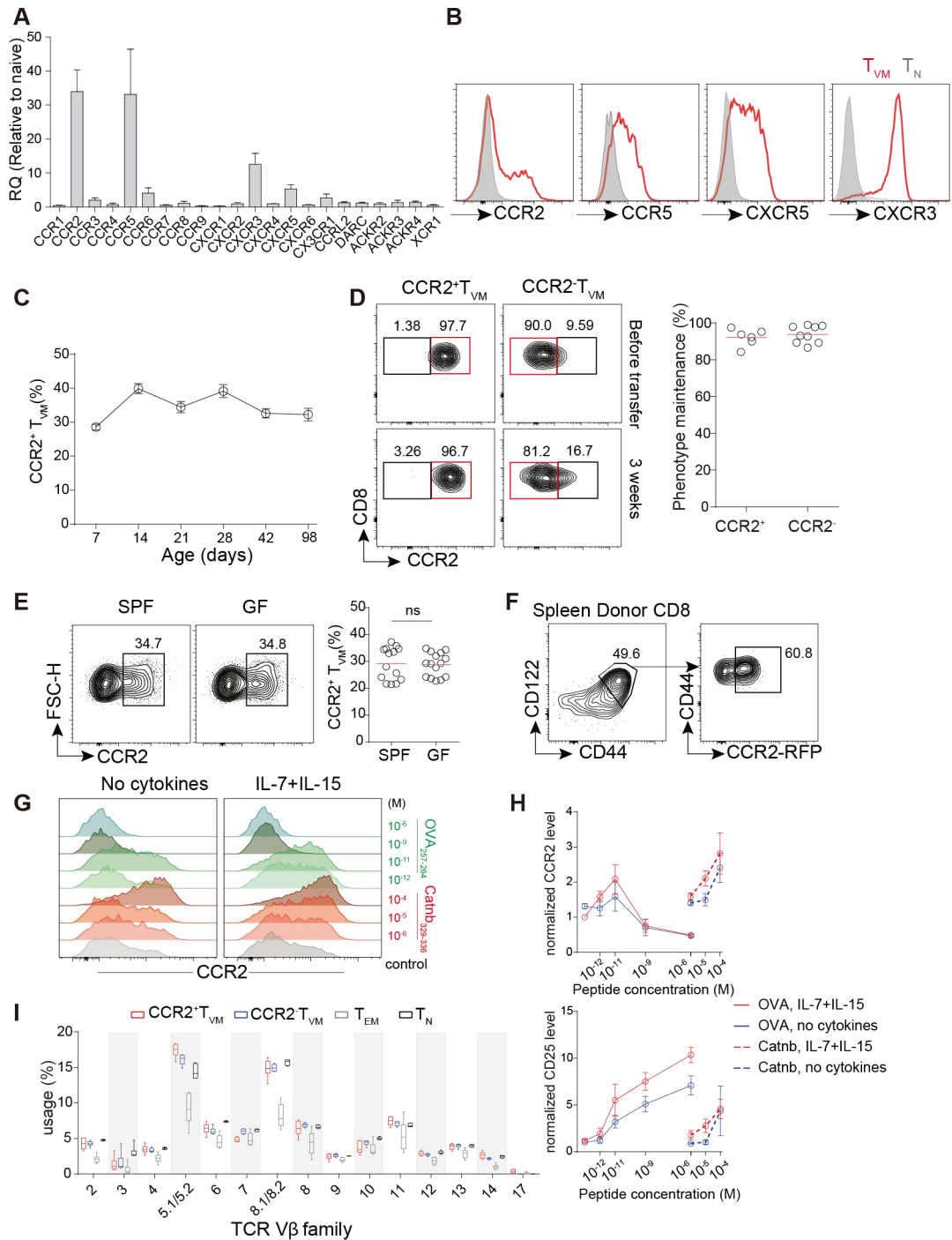
Figure 2

Figure 2. CCR2$^+$ and CCR2$^-$ subsets of virtual memory T cells. (**A**) Expression profiling of chemokine receptors on CD8$^+$ T$_{VM}$ cells (collected from spleen of 6-8 weeks old SPF B6 mice) by quantitative RT-PCR (levels in naïve CD8$^+$ T cells set as 1). Data are mean±s.e.m. of 3 independent experiments. (**B**) Histograms of surface CCR2, CCR5,

CXCR5 and CXCR3 expression on splenic T_{VM} and naïve T (T_N) cells. Representative of 4 independent experiments. (**C**) CCR2$^+$ fraction in splenic T_{VM} cells in B6 mice at indicated ages. Data are presented as mean±s.e.m. of 6 mice at each point. (**D**) Left: representative contour plots of donor CCR2$^+$ or CCR2$^-$ T_{VM} cells that were isolated from *Ccr2*$^{rfp/+}$ knock-in reporter mice, immediately before (top) or 3 weeks after (bottom) adoptive transfer into CD45.1 recipients (3x10^5 per mouse). Right: summary statistics of phenotype maintenance as after-to-before ratio of the percentage points in the red gates. Each symbol represents one mouse, and lines denote the means. Data are pooled from 3 independent experiments. (**E**) Representative CCR2 staining patterns of splenic T_{VM} cells from age- (6-8 weeks old) and sex-matched SPF and germ-free (GF) B6 mice (left) and summary statistics of CCR2$^+$ T_{VM} fractions. Each symbol represents one mouse, and lines denote the means. Data are pooled from 3 independent experiments. n.s., not significant, by unpaired *t* test. (**F**) RFP-reported CCR2 expression on spleen T_{VM} cells generated from naïve *Ccr2*$^{rfp/+}$ T cells, 21 days after being transferred into sublethally irradiated CD45.1 mice. Data representative of 2 independent experiments and 9 mice. (**G**) Representative CCR2 expression profiles, measured by reporter fluorescence, of *Ccr2*$^{rfp/+}$ OT-I T cells after 4-day stimulation with indicated self or agonist peptide in the presence of mitomycin-treated splenic antigen presenting cells, with or without 20 ng/ml IL-7 and IL-15. (**H**) Top: CCR2 levels normalized against the control condition as measured in (G). Bottom: CD25 levels normalized against the control, as detected by antibody surface staining. Data are presented as mean±s.e.m. of the 3 independent experiments. (**I**) TCR Vβ usage as determined by Vβ family-specific antibody staining of indicated cell types in *Ccr2*$^{rfp/+}$ mice. Data are presented as box-whisker plots of 6 mice.
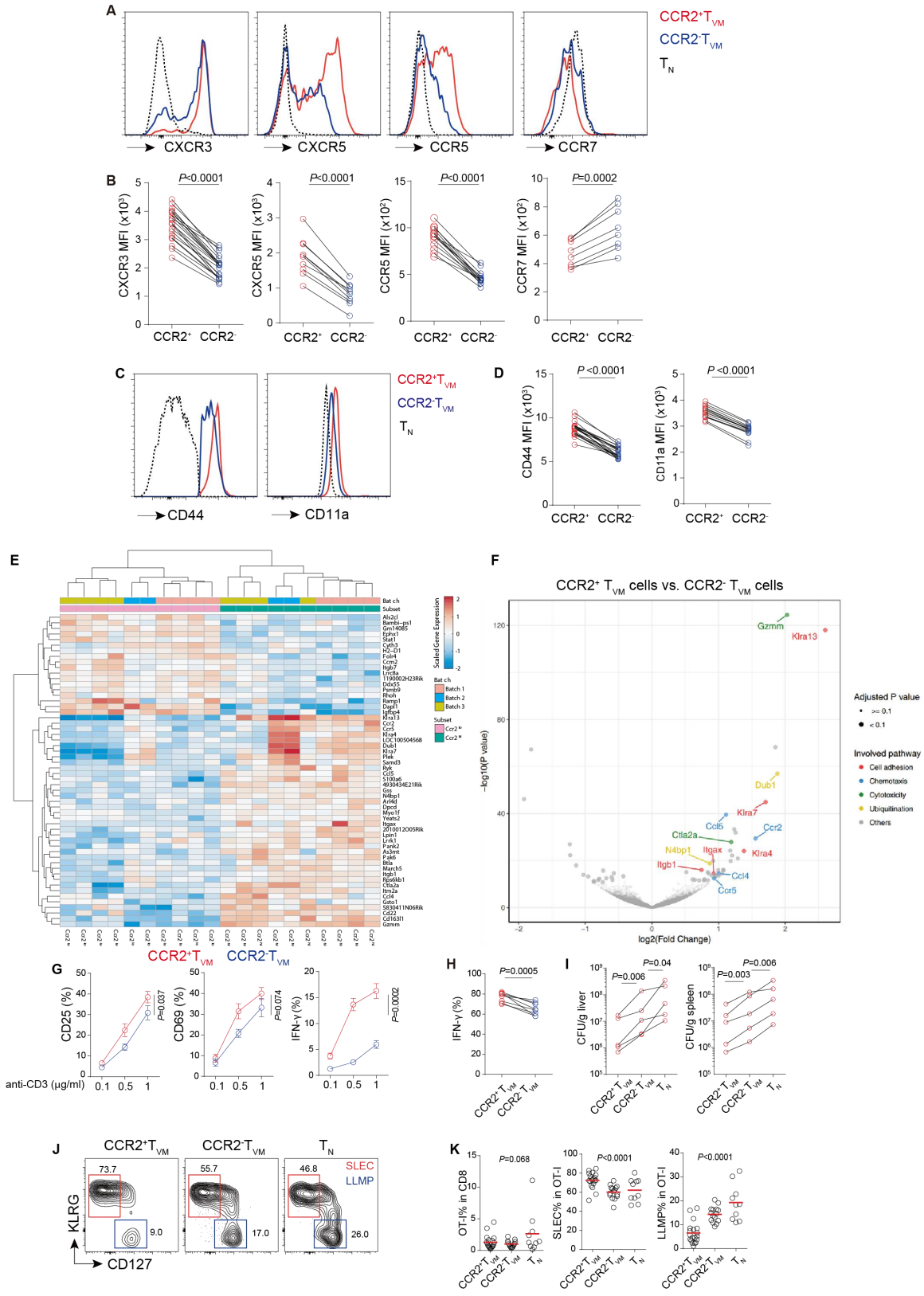
Figure 3

28

Figure 3. Differential expression profiles and functional properties of CCR2$^+$ T$_{VM}$, CCR2$^-$ T$_{VM}$, and naïve T cells.

(**A, B**) Differential expression of chemokine receptor profiles. Representative histograms of indicated chemokine receptors (A) and MFIs of receptor staining on CCR2$^+$ and CCR2$^-$ T$_{VM}$ cells from individual mice (B). Each pair of line-connected dots represent one individual mouse. *P* values by paired *t* tests. (**C, D**) Representative histograms of surface CD44 and CD11a expression on CCR2$^+$ T$_{VM}$, CCR2$^-$ T$_{VM}$ or T$_N$ cells from *Ccr2*$^{rfp/+}$ mice (C). CD44 and CD11a MFI on CCR2$^+$ and CCR2$^-$ T$_{VM}$ cells (D). Each pair of line-connected dots represent one individual mouse; paired *t* tests.

(**E, F**) Transcriptome profiling of CCR2$^+$ and CCR2$^-$ T$_{VM}$ cells. (E) A heatmap of differential expressed genes between CCR2$^+$ and CCR2$^-$ T$_{VM}$ cells from *Ccr2*$^{rfp/+}$ mice, after unsupervised clustering. Ten biological replicates from three independent experiments. (F) Volcano plot of differentially expressed genes, highlighting a set of manually curated genes. (**G**) Frequencies of CCR2$^+$ or CCR2$^-$ T$_{VM}$ cells that were CD25$^+$, CD69$^+$ or intracellular IFN-γ producers after 4h stimulation with indicated concentrations of plate-bound anti-CD3 together with 10 µg/ml anti-CD28. Data (mean±s.e.m. of triplicated wells) from one of 3 independent experiments with similar results are shown. Between-subset comparisons by two-way ANOVA, Bonferroni correction. (**H**) Frequencies of intracellular IFN-γ$^+$ producers in sort-isolated CCR2$^+$ and CCR2$^-$ T$_{VM}$ cells after 16h stimulation with 10 ng/ml IL-12, 10 ng/ml IL-18 and 10U/ml IL-2. Each pair of line-connected dots represent one individual mouse (n=8); paired *t* test. (**I**) Listeria load (CFU) per gram liver or spleen tissue from *Cd8*$^{-/-}$ mice that received CCR2$^+$ T$_{VM}$, CCR2$^-$ T$_{VM}$ or T$_N$ cells, 4 days after *Lm*-OVA (10^5 CFU) infection. Each line represents one of 5 independent experiments, and each dot presents the mean value from 2-3 mice per condition. *P* values by paired *t* tests. (**J**) Representative contour plots of CD45.1$^+$ OT-I donor cells in the spleen 21 days after *Lm*-OVA (10^4 CFU) infection. Numbers indicate percentages of gated cells. (**K**) Summary data of OT-I frequencies in total CD8$^+$ T cells and CD127^{lo}KLRG^{hi} SLEC or CD127^{hi}KLRG^{lo} LLMP frequencies in OT-I cells. Each symbol represents one mouse, and lines denote means. Data are pooled from 4 independent experiments. *P* values by one-way ANOVA.
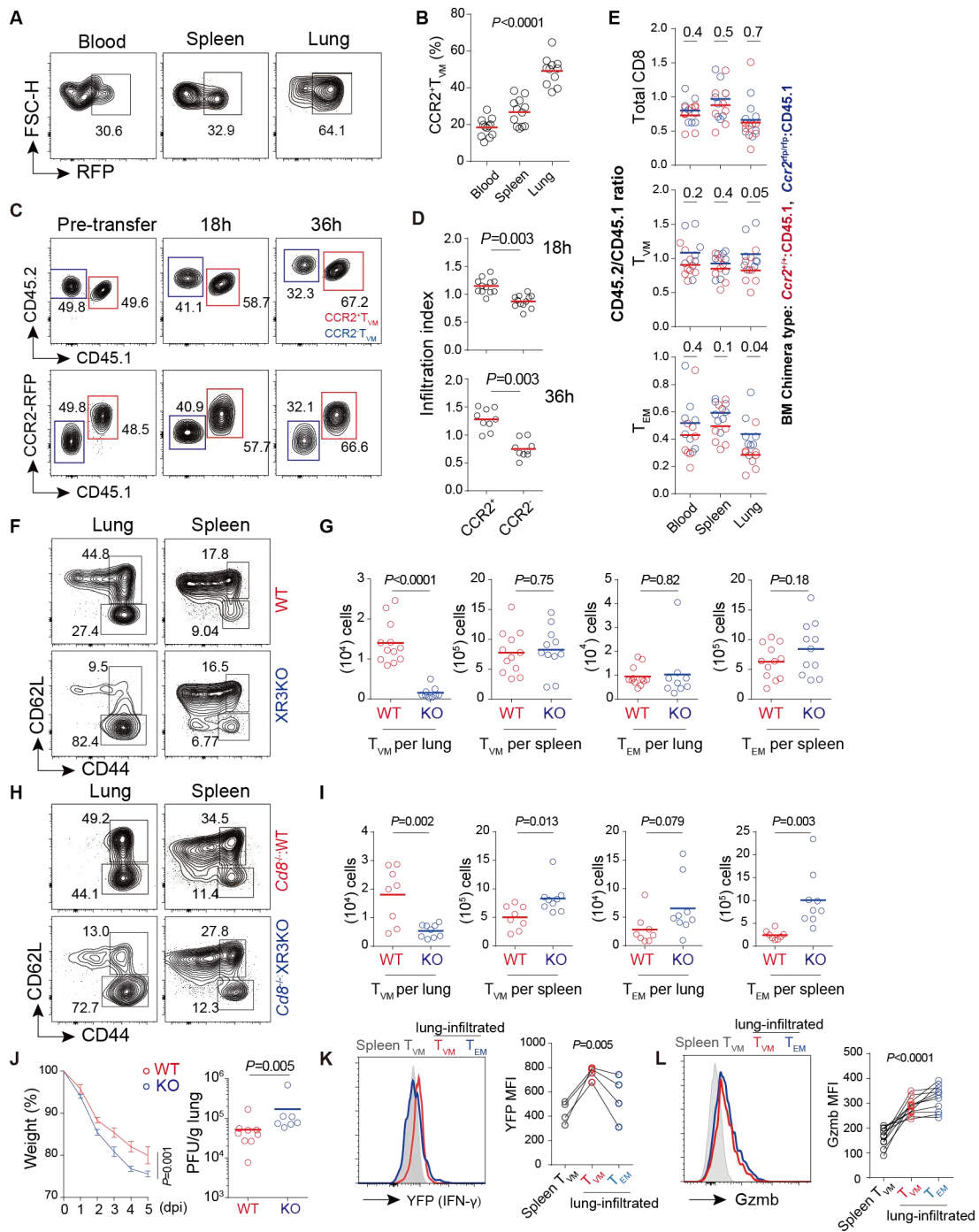
Figure 4

Figure 4. The CCR2$^+$ T$_{VM}$ subset dominates early lung infiltration and promotes viral control. (**A, B**) Representative contour plots (A) and summary data (B) of CCR2$^+$ T$_{VM}$ subset frequencies in the blood, splenic and lung-infiltrated CD8$^+$ T cells in *Ccr2*$^{rfp/+}$ mice one day after PR8 infection (10^4 PFU). Each symbol is one mouse, and lines denote

means. Data are pooled from 3 experiments. *P* values by one-way ANOVA. (**C**) Representative contour plots of pre-transfer mix of sort-purified CD45.1/2 CCR2$^+$ and CD45.2 CCR2$^-$ T$_{VM}$ cells (left) and their respective contributions to lung-infiltrated donor CD8$^+$ T cells 18h (middle) or 36h (right) in PR8-infected CD45.1 mice. CD45.1 vs-CD45.2 and CD45.1-vs-RFP plots of the same representative sample are presented in each column. (**D**) Summary data of infiltration index, calculated as the ratio between post- and pre-transfer frequencies for indicated subsets. Each symbol is one mouse, and lines denote means. Data are pooled from 3 experiments. *P* values by unpaired *t* tests. (**E**) CD45.2/CD45.1 ratios in CD8$^+$ T cells, CD62L$^+$CD44$^+$ T$_{VM}$ cells, or CD62L$^-$CD44$^+$ T$_{EM}$ cells in the blood, spleen or lung-infiltrated cells of mixed BM chimera (1:1 mix of CD45.1 and CD45.2 *Ccr2*$^{+/+}$ or CD45.2 *Ccr2*$^{rfp/rfp}$) that were infected with PR8 (10^4 PFU) 1 day before. Each symbol is one mouse, and lines denote means. Data are pooled from 3 experiments. Numbers above each columns are *P* values by unpaired *t* tests. (**F**) Representative contour plots of lung and splenic CD8$^+$ T cells one day after PR8 (10^4 PFU) infection of littermate WT and CXCR3KO (XR3KO) mice. (**G**) Numbers of cells recovered per lung or spleen from WT or XR3KO mice as in (**F**). Each symbol is one mouse, lines denote means. Data are pooled from 3 experiments. *P* values by unpaired *t* tests. (**H**) Representative contour plots of lung and splenic CD8$^+$ T cells one day after PR8 (10^4 PFU) infection of *Cd8*$^{-/-}$:WT and *Cd8*$^{-/-}$:XR3KO (80:20) chimera. (**I**) Numbers of T$_{VM}$ or T$_{EM}$ cells recovered per lung or spleen from chimeric mice as in (H). Each symbol is one mouse, lines denote means. Data are pooled from 3 experiments. *P* values by unpaired *t* tests. (**J**) Left: weight loss of *Cd8*$^{-/-}$:WT and *Cd8*$^{-/-}$:XR3KO (80:20) chimera that were infected with PR8 (10^4 PFU) and daily treated with FTY720 after 1 day. The body weight before infection is set as 100% (mean±s.e.m., n=10 WT and 8 XR3KO chimera). Between-genotype comparisons by Two-way ANOVA, Bonferroni correction. Right: viral titers in the lung at 5 dpi. Each symbol is one mouse, and lines denote means. Mann-Whitney test. (**K**) Left: representative histograms of IFN-γ reporter fluorescence in indicated cell types from IFN-γ–YFP reporter mice one day after PR8 infection (10^4 PFU). Right: IFN-γ reporter MFI in indicated cell types. Each set of line-connected dots was from one mouse. *P* values by one-way ANOVA. One of two experiments with similar results is shown. (**L**) Left: representative histograms of Granzyme B expression in indicated cell types from B6 mice one day after PR8 infection (10^4 PFU). Right: Granzyme B MFI in indicated cell types. Each set of line-connected dots was from one mouse. *P* values by one-way ANOVA.
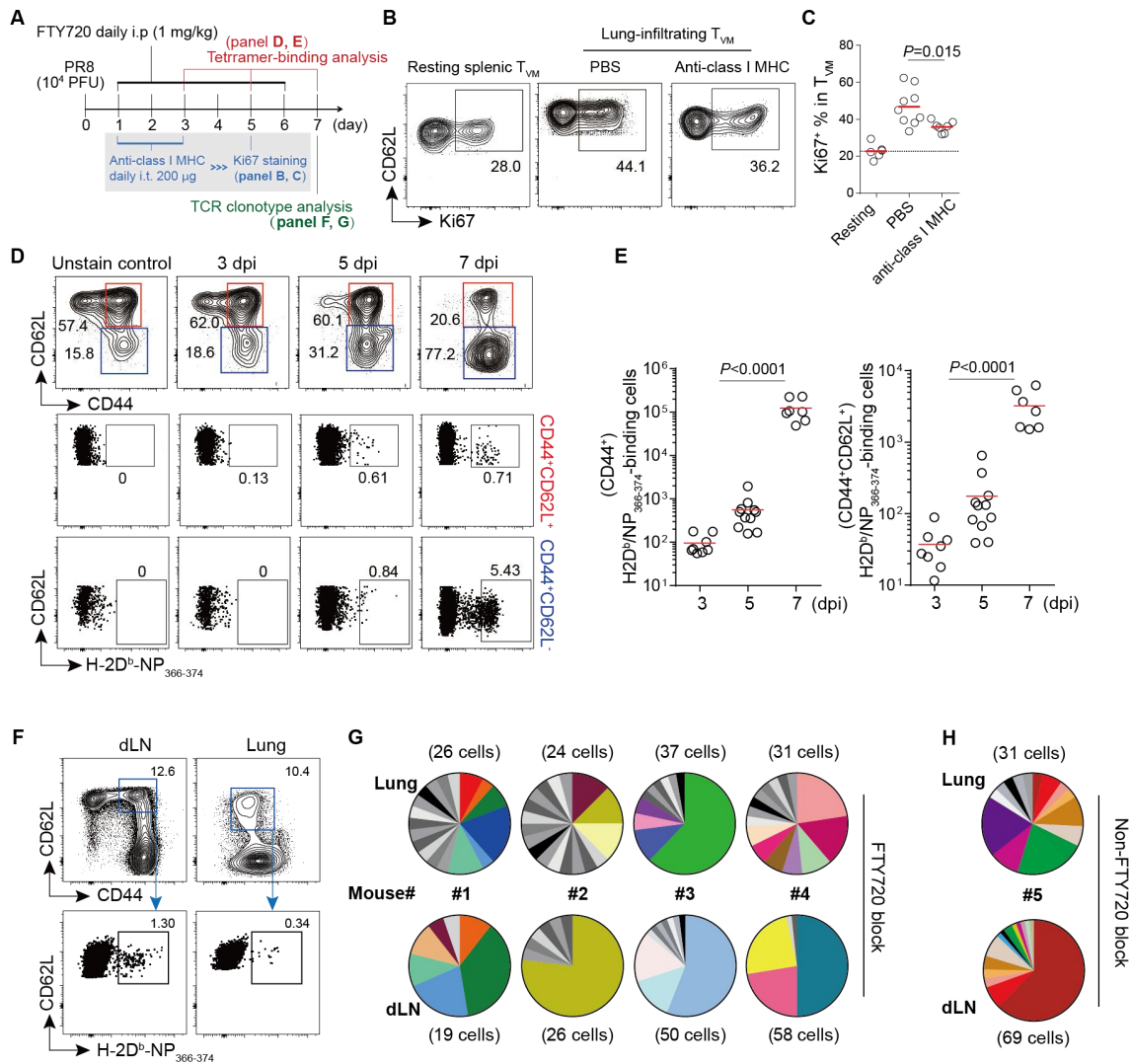
Figure 5

Figure 5. Antigen-specific clonal expansion of T_{VM} cells in the infected lung. (A) Experimental design. The blue-, red-, and green-colored descriptions correspond to indicated figure panels, while procedures in black are universally applied. (**B**) Representative contour plots of Ki67 staining of splenic T_{VM} cells from resting mice or day-5 lung-infiltrated T_{VM} cells from PR8-infected mice that were treated with PBS or anti-class I MHC intratracheally, as described in (A). (**C**) Summary data of Ki67$^+$% in T_{VM} cells of indicated types as in (B). Each symbol is one mouse, lines denote means. Data are pooled from 3 experiments. Unpaired *t* test. (**D**) Representative contour plots of CD44$^+$CD62L$^+$ cells and CD44$^+$CD62L$^+$ H2-D^b/NP$_{366-374}$-binding cells, CD44$^+$CD62L$^-$ and CD44$^+$CD62L$^-$ H2-D^b/NP$_{366-374}$-binding cells analyzed at indicated time post infection. (**E**) Numbers of CD44$^+$ H2-D^b/NP$_{366-374}$-binding cells (left) and those of a CD44$^+$CD62L$^+$ phenotype (right). Each symbol is one mouse, lines denote means. Data

are pooled from 3 experiments. *P* values by one-way ANOVA. (**F**) The sorting scheme for isolating CD62L$^+$CD44$^+$ H2-D^b/NP$_{366-374}$-binding cells from mediastinal LN (dLN) and lung of the same infected mice, as described in (A). (**G**) TCR clonotypes of single H2-D^b/NP$_{366-374}$-binding cells in 4 mice, as isolated in (F). (**H**) TCR clonotypes of single CD62L$^+$CD44$^+$ H2-D^b/NP$_{366-374}$-binding cells isolated from dLN and lung of the same mouse 7 days after PR8 infection (10^4 PFU), without FTY720 blockade. For each mouse described in (F-H), same colors in the two pie charts indicate identical clones shared between the lung and dLN, unique colors indicate clones unique to the lung or dLN, while graded greys denote individual clones with no repeats in either organ. No identical clones were shared between different mice.
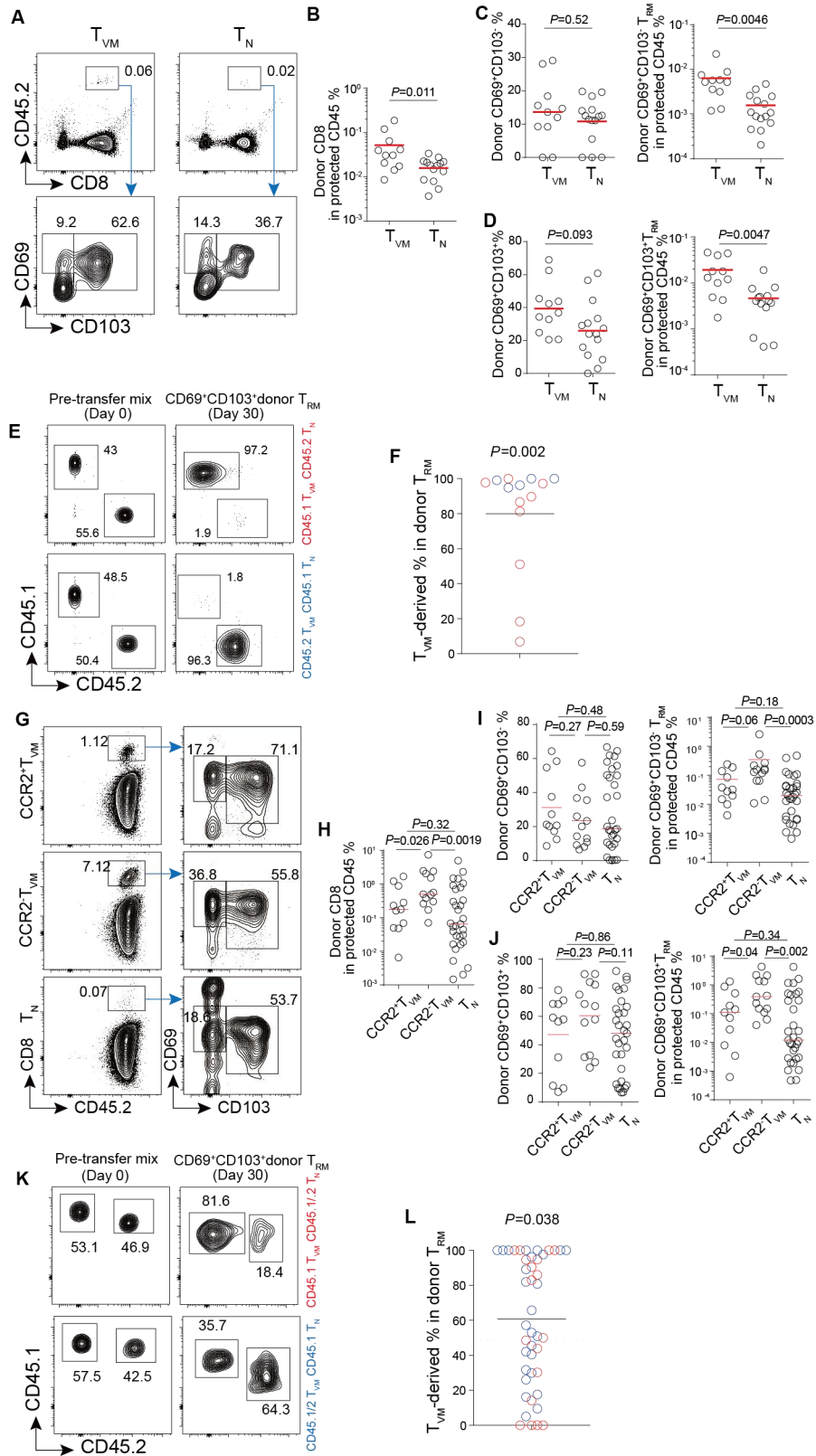
Figure 6

Figure 6. Enhanced T_{RM} development from T_{VM} cells. **(A-D)** Lung T_{RM} development from CD45.2$^+$ T_{VM} or T_N precursors (3×10^5 per CD45.1 recipient before 50 PFU PR8 infection). (A) Representative contour plots of donor-derived CD8$^+$ T cells (top) and T_{RM} cells (bottom) in the lung. (B) Donor CD8$^+$ T cell abundance in the lung, measured as the fraction of total resident CD45$^+$ cells. CD69$^+$CD103$^-$% (C) or CD69$^+$CD103$^+$% (D) in the donor CD8$^+$ T cell compartment (left) or abundance in the lung, measured as the fraction of total resident CD45$^+$ cells (right). Each symbol is one mouse, lines denote means. Data are pooled from 4 experiments. *P* values by Mann-Whitney tests. **(E, F)** Lung T_{RM} development from competing T_{VM} and T_N precursors (1:1 CD45.1 T_{VM} vs CD45.2 T_N (red symbols) or vice versa (blue symbols), 3×10^5 per *Cd8$^{-/-}$* recipient before 20 PFU PR8 infection). Representative contour plots of pre-transfer mix or the CD69$^+$CD103$^+$ T_{RM} compartment derived from the donor cells (E) and a scatter plot to show T_{VM}-derived T_{RM} fractions in individual recipients (F). Each symbol is one mouse, and red line indicates the mean. Dotted line highlights the input ratio, which is expected by the null hypothesis scenario; rejected by *t* test. **(G-J)** Lung T_{RM} development from CCR2$^+$ T_{VM}, CCR2$^-$ T_{VM}, or T_N precursors (3×10^5 per *Cd8$^{-/-}$* recipient before 20 PFU PR8 infection). (G) Representative contour plots of donor-derived CD8$^+$ T cells (left) and T_{RM} cells (right) in the lung. (H) Donor CD8$^+$ T cell abundance in the lung, measured as the fraction of total resident CD45$^+$ cells. CD69$^+$CD103$^-$% (I) or CD69$^+$CD103$^+$% (J) in the donor CD8$^+$ T cell compartment (left) or abundance in the lung, measured as the fraction of total resident CD45$^+$ cells (right). Each symbol is one mouse, lines denote means. Data are pooled from 5 experiments. *P* values by Mann-Whitney tests. **(K, L)** Lung T_{RM} development from competing OT-I T_{VM} and T_N precursors (1:1 CD45.1 T_{VM} vs CD45.1/2 T_N (red symbols) or vice versa (blue symbols), 40 cells of each type per B6 recipient before 100 PFU PR8-OVA infection). Representative contour plots of pre-transfer mix or the CD69$^+$CD103$^+$ T_{RM} compartment derived from the donor cells (K) and a scatter plot to show T_{VM}-derived T_{RM} fractions in individual recipients (L). Each symbol is one mouse, and red line indicates the mean. Dotted line highlights the input ratio, which is expected by the null hypothesis scenario; rejected by *t* test.

Supplementary Materials for

Virtual memory T-cells orchestrate extra-lymphoid responses

conducive to resident memory

Shiyue Hou[1,2,3]†, Tiange Shao[1,2,3]†, Tianyang Mao[4], Jingwen Shi[1,2,3,4], Jiahui Sun[1,2,3], Miao Mei[1,5], Xu Tan[1,5], Hai Qi[1,2,3,4,6,7]*

Correspondence to: qihai@tsinghua.edu.cn

This file includes:

Figures S1 to S7

Other Supplementary Materials for this manuscript include the following:

Table S1 [Excel file containing 5 spreadsheets, providing TCR sequence reads]
Table S2 [Excel file containing 5 spreadsheets, providing primers used for TCR sequence analyses]
Table S3 [Excel file containing 1 spreadsheet, providing raw data used to generate all graphs]
Table S4 [Excel file containing 1 spreadsheet, providing RT-PCR primers used for chemokine receptor screening]
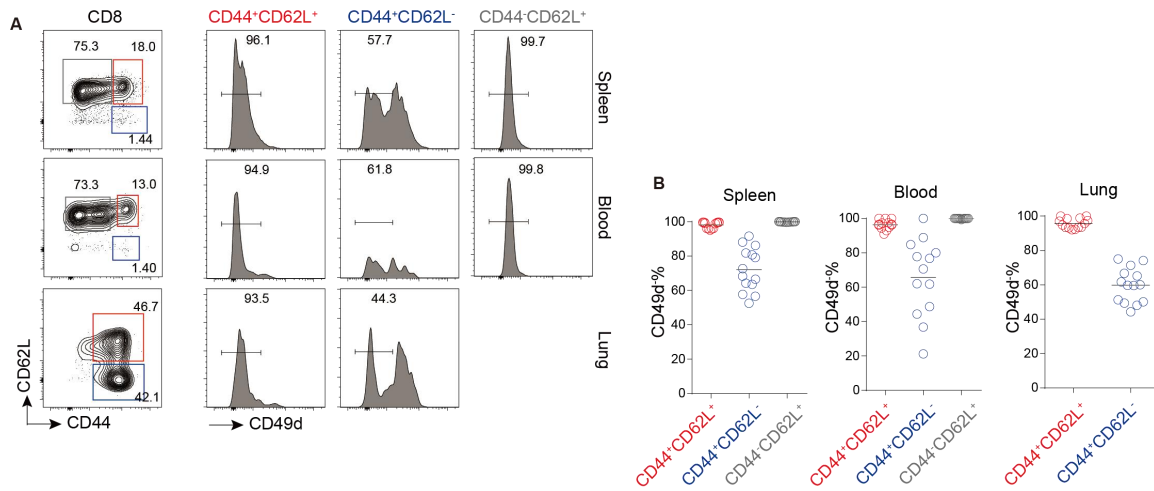
Figure S1. Development of CCR2$^+$ T$_{VM}$ cells.

(**A, B**) Representative profiles (A) and summary statistics (B) of CD49d$^-$ proportion in T cells of CD44$^-$CD62L$^+$ (gate in grey), CD44$^+$CD62L$^+$ (gate in red), and CD44$^+$ CD62L$^-$ (gate in blue) phenotype from the spleen, blood and lung (gated on CD45 i.v.$^-$ cells) 1 day after flu infection. In all scatter plots, one dot represents one mouse, and lines denote means; data were pooled from 3 independent experiments; *P* values by unpaired *t* tests.

Figure S2
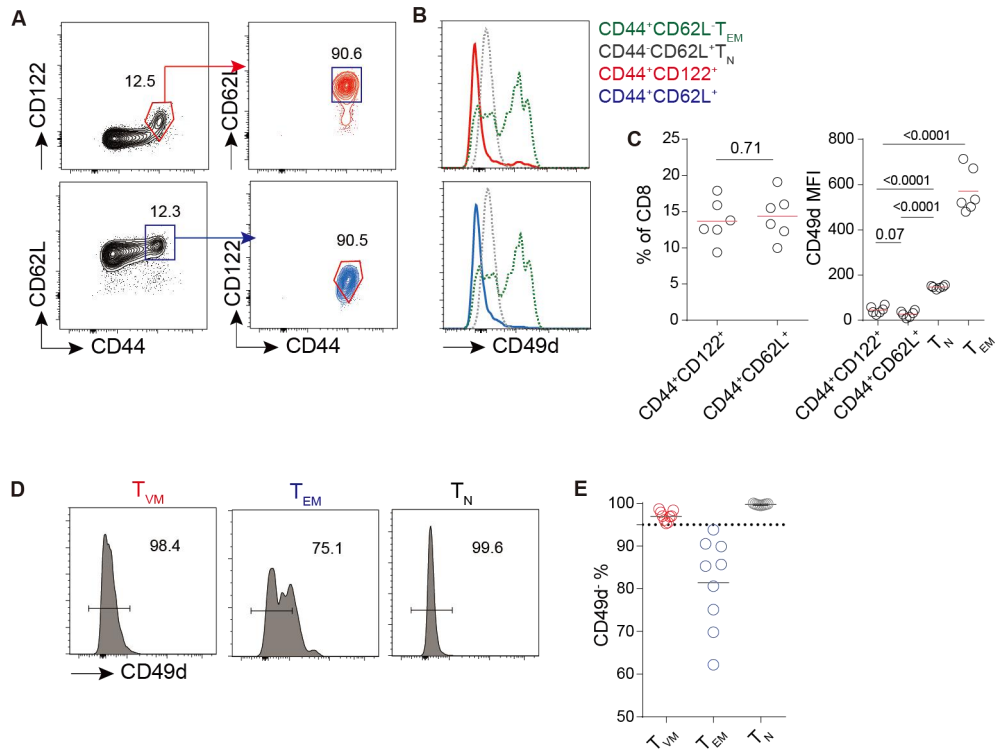
Figure S2. Characterization of T$_{VM}$ cells

(**A**) Representative contour plots of two T$_{VM}$-gating strategies in 6-8 week old SPF mice, CD44$^+$CD122$^+$ and CD44$^+$CD62L$^+$. (**B**) Representative histograms of CD49d expression, gated in the two different ways as in (A). (**C**) Left, summary statistics of T$_{VM}$ frequencies, gated in the two different ways as in (A); Right, mean fluorescent intensity (MFI) of CD49d expression, gated in the two different ways as in (A), in comparison to CD44$^+$CD62L$^-$ T$_{EM}$ cells and CD44$^-$CD62L$^+$ T$_N$ cells. In all scatter plots, one dot represents one mouse, and lines denote means; data were pooled from 3 independent experiments; *P* values by unpaired *t* tests. (**D, E**) Representative histograms (D) and summary statistics (E) of CD49d$^-$ cells in CD62L$^+$CD44$^-$ T$_N$, CD62L$^+$CD44$^+$ T$_{VM}$, and CD62L$^-$CD44$^+$ T$_{EM}$ phenotype from the spleen of 6- to 8-week-old SPF mice. One dot represents one mouse, and lines denote means; data were pooled from 2 independent experiments; *P* values by unpaired *t* tests.
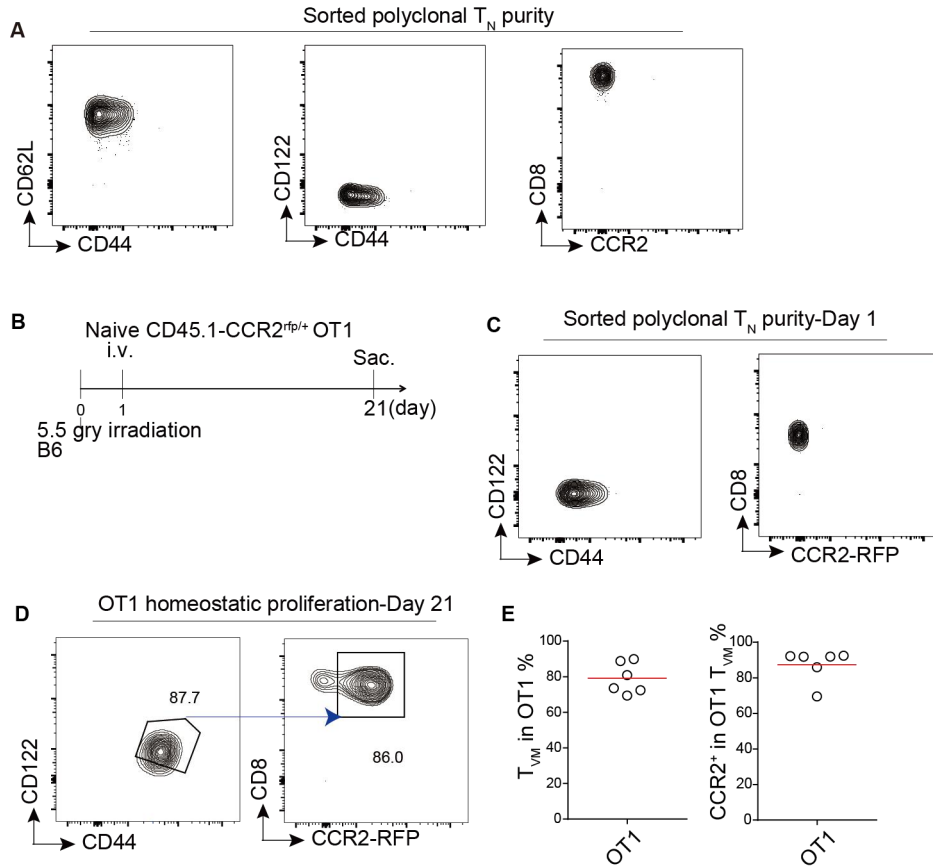
Figure S3. Generation of CCR2$^+$T$_{VM}$ cells by homeostatic proliferation

(**A**) Representative counter plots of sort-purified *Ccr2*$^{rfp/+}$ naïve T cells before transfer into irradiated recipients for measuring homeostatic proliferation in Figure 2F. (**B**) Workflow for examining homeostatic proliferation of naïve OT-I T cells. (**C**) Contour plots of the sort-purified CD45.1 *Ccr2*$^{rfp/+}$ OT-I naïve T cells. (**D, E**) Representative profiles (D) and summary statistics (E) of RFP-reported CCR2 expression on T$_{VM}$ cells generated from naïve *Ccr2*$^{rfp/+}$ OT-I T cells, 21 days after being transferred into sublethally irradiated CD45.1 mice.
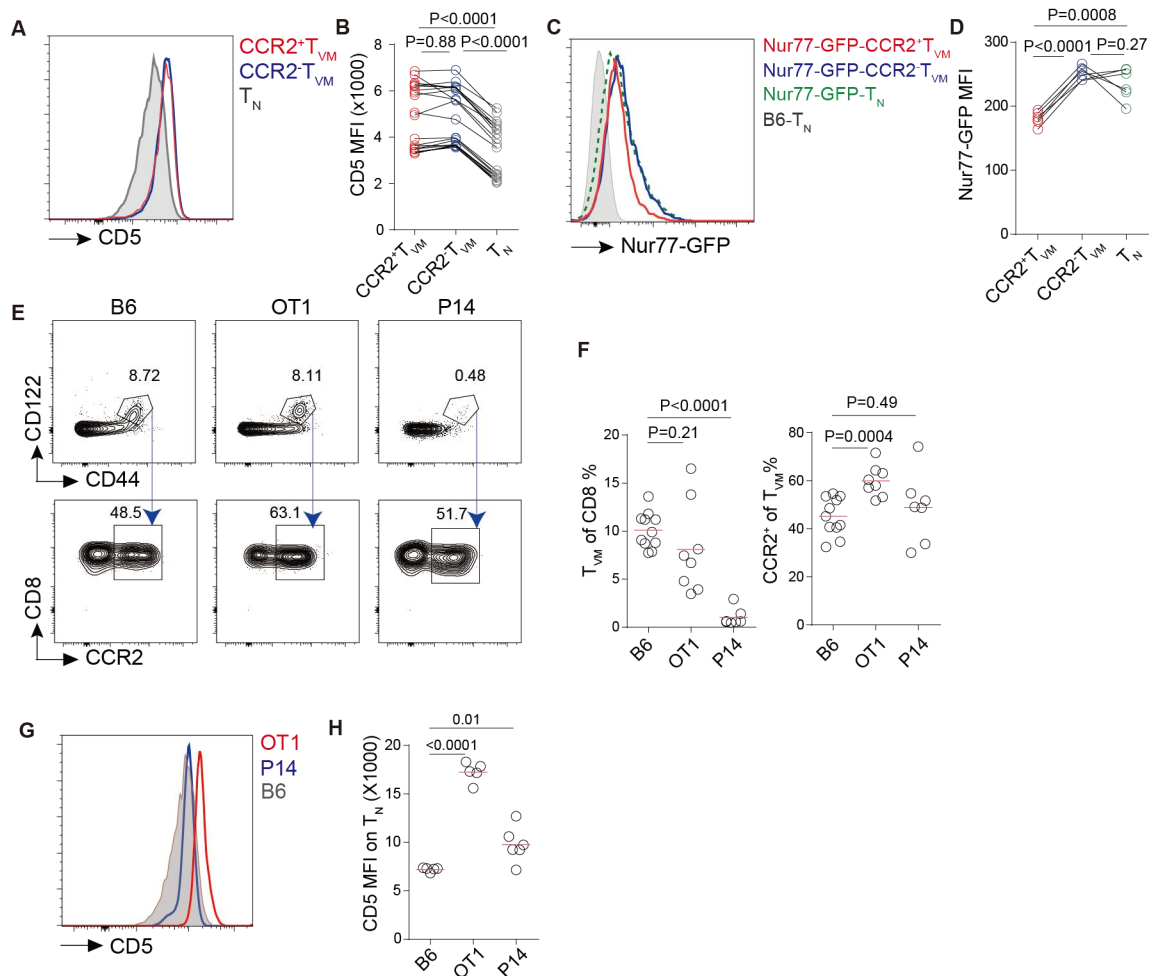
Figure S4. CD5 and Nur77 expression in CCR2$^+$ and CCR2$^-$ T$_{VM}$ cells

(**A, B**) Representative histograms (A) and MFI (B) of CD5 expression by CCR2$^+$ and CCR2$^-$ T$_{VM}$ and T$_N$ cells from *Ccr2*$^{rfp/+}$ mice. Each pair of line-connected dots represent one individual mouse. *P* values by paired *t* tests. (**C, D**) Representative histograms (C) and MFI (D) of Nur77-GFP expression by CCR2$^+$ and CCR2$^-$ T$_{VM}$ and T$_N$ cells from Nur77-GFP×*Ccr2*$^{rfp/+}$ mice. T$_N$ cells from B6 mice were used as negative control. Each pair of line-connected dots represent one individual mouse. *P* values by paired *t* tests. (**E, F**) Representative profiles (E) and summary statistics (F) of CD44$^+$CD122$^+$ T$_{VM}$ cells and CCR2$^+$ T$_{VM}$ cells from B6, OT-I, and P14 mice (6-8 weeks of age). One dot represents one mouse, and lines denote means; data were pooled from 3 independent experiments; *P* values by unpaired *t* tests. (**G, H**) Representative histograms (G) and MFI statistics (H) of CD5 expression by CD44$^-$CD122$^-$ T$_N$ cells from B6, OT-I and P14 mice. One dot represents one mouse, and lines denote means; data were pooled from 2 independent experiments; *P* values by unpaired *t* tests.
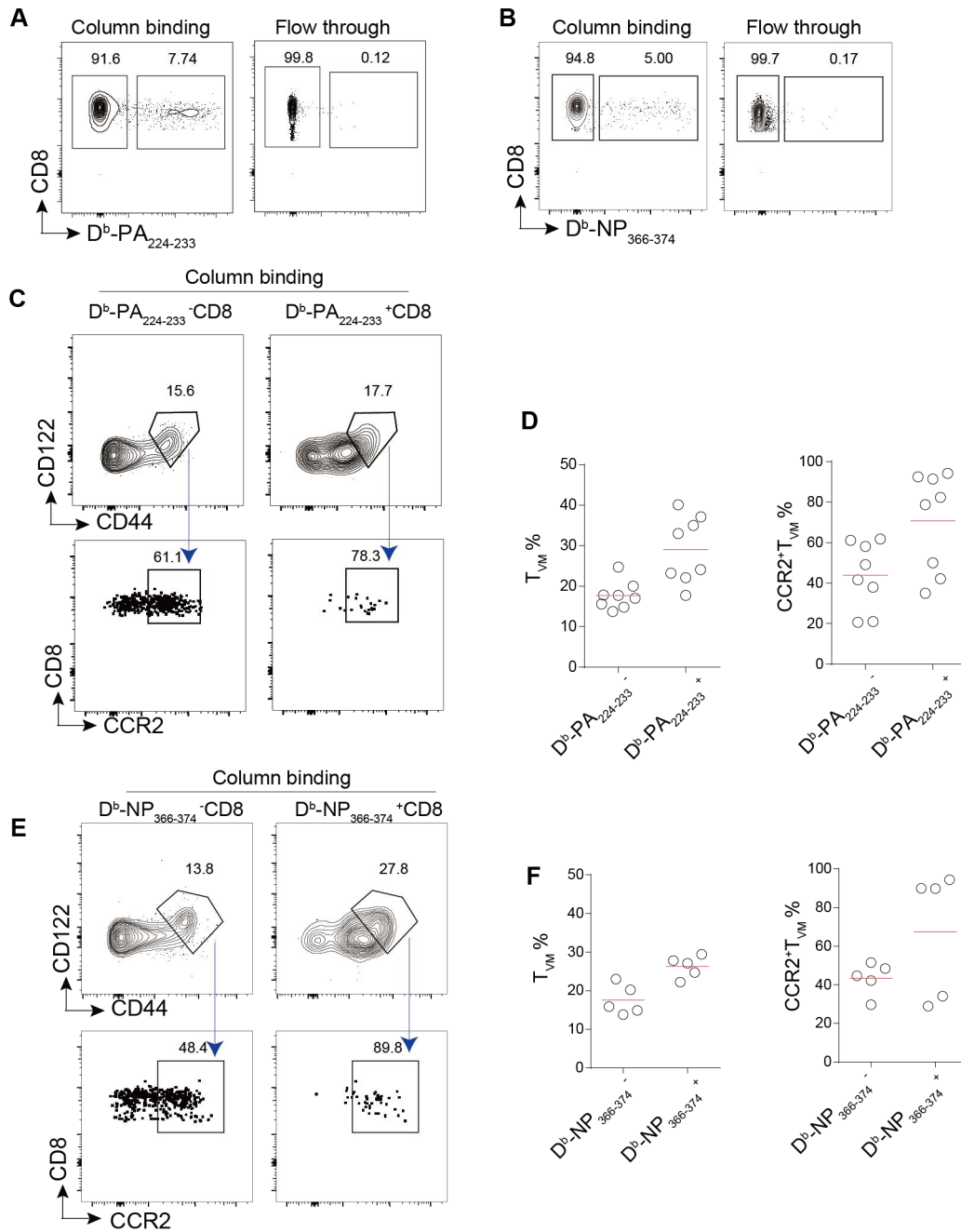
Figure S5

Figure S5. CCR2$^+$ T$_{VM}$ population in tetramer-binding precursors in naïve mice.
(**A, B**) Representative profiles of D^b-PA$_{224-233}$- (A) and D^b-NP$_{366-374}$-binding (B) cells
after tetramer-binding enrichment. (**C, D**) Representative profiles (C) and summary
statistics (D) of CD44$^+$CD122$^+$ T$_{VM}$% (D, Left) and CCR2$^+$% in T$_{VM}$ cells (D, Right) in
the D^b-PA$_{224-233}$ group. Tetramer-negative cells were used as the respective polyclonal

control. One dot represents one mouse, and lines denote means; data were pooled from 3 independent experiments. (**E, F**) Representative profiles (C) and summary statistics (D) of $CD44^+CD122^+$ T_{VM}% (D, Left) and $CCR2^{+\circ}$% in T_{VM} cells (D, Right) in the D^b-$NP_{366-374}$ group. Tetramer-negative cells were used as the respective polyclonal control. One dot represents one mouse, and lines denote means; data were pooled from 2 independent experiments.
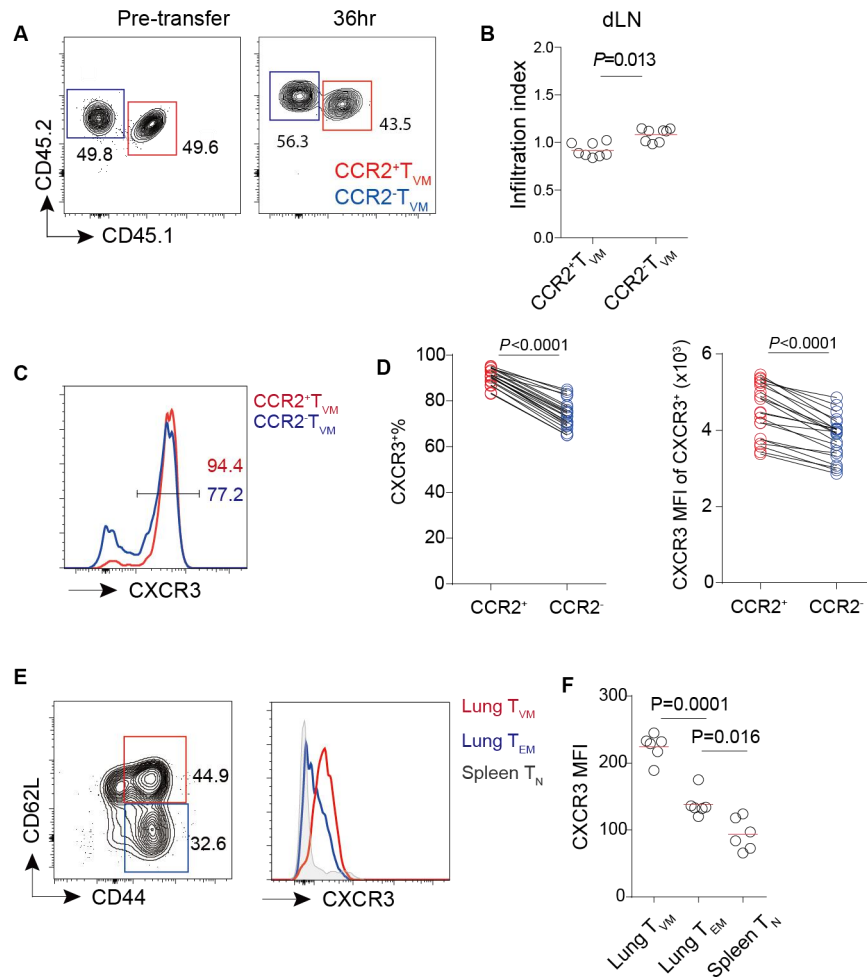
Figure S6

Figure S6. The $CCR2^+$ T_{VM} subset dominates early lung infiltration with high CXCR3 expression.

(**A**) Representative contour plots of pre-transfer mix of sort-purified CD45.1/2 $CCR2^+$ and CD45.2 $CCR2^-$ T_{VM} cells (left) and their respective contribution in donor CD8 T cells in dLN (right) 36 h after PR8 infection of CD45.1 hosts (corresponding experiment in Fig. 4C). (**B**) Summary data of infiltration index, calculated as the ratio between post- and

pre-transfer frequencies for indicated subsets. Each symbol is one mouse, and lines denote means. Data are pooled from 3 experiments. *P* values by unpaired *t* tests. **(C)** Representative CXCR3 histograms of indicated T_{VM} subsets from naïve *Ccr2*[rfp/+] mice. **(D)** Summary statistics of CXCR3$^+$ frequencies and MFI of CXCR3 expression on CXCR3$^+$ cells of the indicated T_{VM} subsets from naïve *Ccr2*[rfp/+] mice. Each pair of line-connected dots represent one individual mouse. *P* values by paired *t* tests. **(E)** Representative gating of lung-infiltrating CD44$^+$CD62L$^+$ T_{VM} and CD44$^+$CD62L$^-$ T_{EM} cells (left) and histograms of CXCR3 expression by these cells (right) 1 day after PR8 infection. **(F)** Summary statistics of CXCR3 MFI on lung-infiltrating CD44$^+$CD62L$^+$ T_{VM} and CD44$^+$CD62L$^-$ T_{EM} cells, gated as in (E), with splenic CD44$^-$CD62L$^+$ T_N cells from the same mice used as a control. Each dot represents one mouse, and lines denote means; data were pooled from 2 independent experiments; *P* values by unpaired *t* tests.
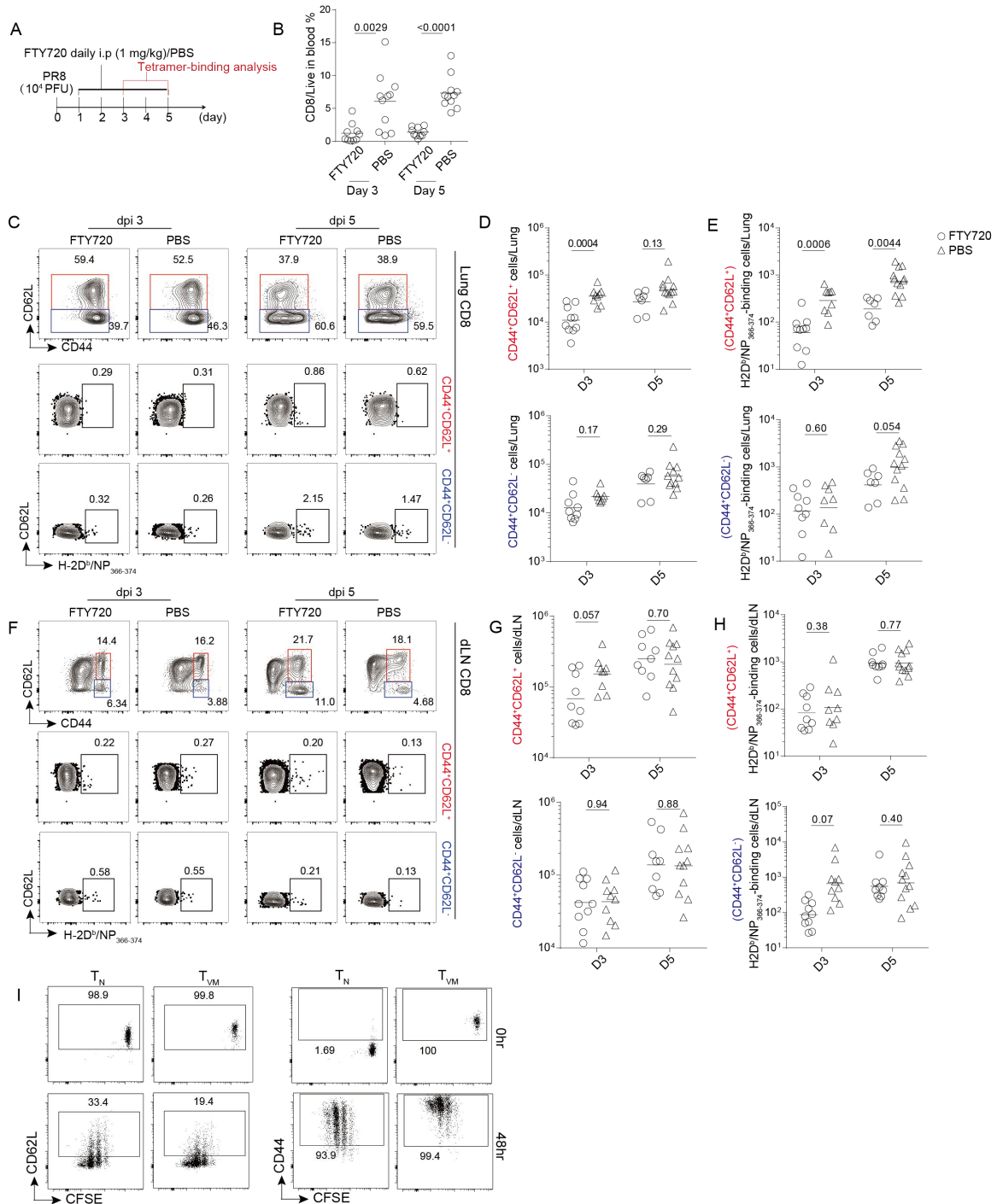
Figure S7. Antigen-specific expansion of T_{VM} cells in situ.

(**A**) The experimental schedule. (**B**) Summary statistics of abundance of CD8 T cells in blood with or without FTY720 blockade at indicated times. (**C-E**) Representative contour plots (**C**) and summary statistics (D, E) of indicated lung CD8 T cells. (**C**) Top, lung CD8

T cells gated for CD44$^+$CD62L$^+$ (in red) and CD44$^+$CD62L$^-$ (in blue); middle, H2-D^b/NP$_{366-374}$-binding cells in CD44$^+$CD62L$^+$; bottom, H2-D^b/NP$_{366-374}$-binding cells in CD44$^+$CD62L$^-$. (**D, E**) Numbers of lung CD44$^+$CD62L$^+$ (top) or CD44$^+$CD62L$^-$ (bottom) CD8 T cells (D) and H2-D^b/NP$_{366-374}$-binding CD8 T cells (E) in the presence of FTY720 blockade (circle) or PBS treatment (triangle). (**F-H**) Representative contour plots (F) and summary statistics (G, H) of indicated dLN CD8 T cells. Panels laid out exactly as in (C-E). (D-E, G-H) Each symbol is one mouse, lines denote means. Data are pooled from 3 experiments. *P* values by unpaired *t* tests. (**I**) CFSE dilution and CD62L downregulation and CD44 upregulation of T$_N$ and T$_{VM}$ cells stimulated for 48 h with plate bound anti CD3 and anti-CD28. Data from one of 3 independent experiments with similar results are shown.